Raman Mapping as a Tool for Evaluating the I2 and I3– Diffusion Over Single-Crystal UiO-67_NH2(M) (M = Zr, Zr/Hf, or Hf)

Pedro Andrade, Myriam Moreau, Natacha Henry, Mohamed-Taieb Bakouche, Sylvain Duval, Christophe Volkringer, Thierry Loiseau, Matthieu Hureau, Alain Moissette

▶ **To cite this version:**

HAL Id: hal-04044389
https://hal.univ-lille.fr/hal-04044389v1

Submitted on 24 Mar 2023

Raman Mapping as a Tool for Evaluating the I_2 and I_3^- Diffusion Over Single-Crystal UiO-67_NH2(M) (M = Zr, Zr/Hf, or Hf)

Pedro H. M. Andrade[1,*], Myriam Moreau[1], Natacha Henry[2], Mohamed T. Bakouche[2], Sylvain Duval[2], Christophe Volkringer[2], Thierry Loiseau[2], Matthieu Hureau[1], Alain Moissette[1,★]

(1) Laboratoire de Spectroscopie pour les Interactions, la Réactivité et l'Environnement (LASIRE), Université de Lille – Sciences et Technologies, 59655 - Villeneuve d'Ascq, France.

(2) Unité de Catalyse et Chimie du Solide (UCCS), Univ. Lille, CNRS, Centrale Lille, Univ. Artois, UMR 8181 - UCCS, F-59000 Lille, France

* pedro.moraisandrade@univ-lille.fr – ORCID: 0000-0002-8264-1818

★ alain.moissette@univ-lille.fr – ORCID: 0000-0003-2713-5143

1

ABSTRACT

The capture of gaseous iodine has been deeply studied for trying to mitigate the dangers of nuclear power energy. The UiO family of MOF materials is considered as one of the best candidates for such purpose since it couples high specific surface areas, facility to be chemically modified, great iodine adsorption capacity, and good stability under nuclear accidents conditions. UiO-66 was profoundly evaluated in several works for trapping I_2 by using different linkers and metal contents. A transformation of the I_2 molecule into I_3^- inside such porous systems was verified in other studies and is yet to be better elucidated. The comprehension of this transformation can improve the systems used to capture iodine species and guarantee a better stabilization of such pollutants in a long term. For this reason, three UiO-67_NH_2 samples with different metal contents (Zr, Zr/Hf, and Hf) were employed to capture iodine and the signature of the different species were evaluated using Raman spectroscopy mappings in and out of resonance conditions (λ_{ex} = 515, 633 and 785 nm). The UiO-67_NH_2(Hf) compound demonstrated the best adsorption capacity after 48 h of contact with gaseous I_2 under room temperature, capturing 3428 g.mol^{-1} of iodine. The other two samples, UiO-67_NH_2(Zr/Hf) and UiO-67_NH_2(Zr), adsorbed 2835 g.mol^{-1} and 1658 g.mol^{-1} in the same conditions, respectively. The I_2 transformation into I_3^- was confirmed by the presence of bands related to "perturbed" I_2 and I_3^- at about 170 and 107 cm^{-1}, respectively. The Raman mapping demonstrated that both the monometallic UiO-67_NH_2 samples displayed a homogeneous distribution of the two species after 48 hours of contact with the iodine gas flow, whereas the bimetallic sample exhibited zones with different concentrations of I_2 and I_3^-. This effect was related to the I_2 diffusion process through the UiO-67_NH_2 crystallites, which could be faster in the monometallic UiO-67_NH_2 samples because of their smaller crystal size ($\varnothing \approx 44$ μm and $\varnothing \approx 51$ μm for UiO-67_NH_2(Hf) and UiO-67_NH_2(Zr), respectively) when compared to the UiO-67_NH_2(Zr/Hf) sample ($\varnothing \approx 140$ μm). This paper shows the spatial distribution of I_2 and I_3^- along the crystals of UiO-67_NH_2 materials and correlates this data with the diffusion process of both species, improving the understanding of the mechanism responsible for the iodine conversion and stabilization in UiO materials.

1. INTRODUCTION

The release of radioactive iodine into the atmosphere has become an issue of great concern from the scientific community in the last few decades. This element can be liberated either by nuclear spills, as in the case of Chernobyl and Fukushima accidents, but also during the reprocessing of Spent Nuclear Fuel (SNF) [1,2]. In both cases, the radioactive iodine can be released in its gaseous form (I_2), in which the main radioactive isotopes present are found to be ^{129}I and ^{131}I. While ^{129}I raises concern due to its long half-life time ($t_{1/2} = 1.6 \times 10^7$ years) [3], the ^{131}I is problematic due to its high specific activity (4.59×10^{15} Bq.g^{-1}) [4]. The capture of these isotopes in its gaseous form poses various challenges specially due to its great oxidation capacity at the same time that it can easily spread throughout different ecosystems [5].

The use of Metal-Organic Frameworks (MOFs) materials for the capture of iodine is subject of several studies nowadays [6–8]. MOFs pose enormous advantages compared to other materials due to their high Specific Surface Areas (SSA) (up to 10,000 m^2.g^{-1}), to their enormous range of possible metal-linker combinations (which result in the construction of a plethora of structural architectures), and also to their ability to be chemically functionalized [9,10]. In fact, the optimization of MOF materials for trapping iodine can be achieved by several means such as introducing functional groups, shaping their porosity, using redox metal centers, and doping with metals or active molecules [11]. For instance, since I_2 is known to be an electron acceptor, frameworks with electron donor groups can improve the iodine uptake [6]. Tailoring the size of the pores by using series of iso-reticular MOFs is also an interesting approach for capturing I_2 [11]. An example is a series of Zr-based UiO-66 MOFs that were elongated using linkers containing unsaturated alkene and alkyne as bridges [12]. These materials can improve the iodine uptake by providing sites for the halogenation of their unsaturated C–C bonds [11,12]. Indeed, UiO family of MOFs bearing zirconium stands out in this vast class of crystalline solids due to its thermal and chemical stability as well as its facility to be functionalized, either by replacing the organic linker on its structure or also by changing the metal within the inorganic cluster [6,8] .

For instance, Leloire *et al.* demonstrated the stability of UiO-66_NH$_2$ binderless granules MOF under conditions that simulates a nuclear accident (^{131}I leaking with steam at 120 ºC and up to 2 MGy γ radiation from ^{60}Co source) [7]. In another work, the authors highlighted the influence of modifying the UiO organic linker over the capture of I$_2$, indicating that the presence of –NH$_2$ groups improved the iodine capture by a 2.7 and a 5.5 factor in UiO-66 and UiO-67 series, respectively [6]. Similarly, other functional groups such as –OH and –COOH also favorized the I$_2$ capture [13]. The formation of I$_3^-$ in MOFs after the contact with iodine was reported in several works before [14–16]. In some cases, the reduction of I$_2$ molecules was ascribed to an oxidation of the metallic sites from the framework. For instance, Zhang *et al.* demonstrated that V^{III} centers in MFM-300 can trigger a host-to-guest charge transfer, which oxidates them into V^{IV} and generates I$_3^-$ from I$_2$ molecules [16]. However, recently, Leloire *et al.* [6] demonstrated that there is no redox phenomena related to the zirconium centers in the UiO framework during the I$_3^-$ formation. This feature was later confirmed in another study that evaluated the influence of the metal content (zirconium of hafnium) on the iodine evolution [8]. In fact, considering the isoreticular UiO-66 structure with different metals (Zr and Hf), it was demonstrated that the occurrence of a smaller band gap, coupled with more acidic elements (such as hafnium instead of zirconium) improved the I$_2$ uptake and the I$_3^-$ stabilization in UiO materials [8]. In this case, the I$_3^-$ formation was ascribed to an electron donor-acceptor complex between the 1,4-benzenedicarboxylate (BDC) linker and the I$_2$ molecules, forming a BDC$^{•+}$ radical [8]. It is worth mentioning that benzene-carboxylates cation radicals were already reported in other works, supporting such hypothesis [17,18].

Among the different isoreticular structures that can be obtained with the UiO family, the UiO-67_NH$_2$ member stands out due to its ability to form single crystals with up to 40 µm size [6]. Moreover, although the zirconium based UiO-67_NH$_2$ is easily found in the literature for capturing I$_2$, to the best of the authors' knowledge, there is no mention of a hafnium-doped UiO-67_NH$_2$ being used for such purposes. Nevertheless, UiO-67_NH$_2$(Zr) was found to be one of the best candidates among UiO compounds to adsorb gaseous iodine after 48 hours of exposure (with an I$_2$ uptake capacity of 1071 mg.g^{-1} in dynamic conditions) [6]. Therefore, it is of great interest to evaluate the I$_2$ capture by UiO-67_NH$_2$ with different metal (Zr/Hf) compositions by coupling the best materials for iodine capture and I$_3^-$ stabilization from the two previous studies regarding I$_2$@UiO

4

compounds [6,8]. For this reason, the present contribution focuses on adsorbing gaseous iodine in UiO-67_NH$_2$ compounds with three metal compositions: zirconium, hafnium, and a mixture of zirconium and hafnium (1/1 molar ratio). Apart the classical structural and textural characterizations (XRD, BET, SEM), this study was mainly conducted by using different vibrational (IR, Raman) and adsorption (UV-Vis) spectroscopies. In particular Raman spectroscopy was able to produce 2D and 3D mapping by means of different wavelength excitation sources (515, 633, and 785 nm) in order to probe the encapsulated iodine molecules. In this way, resonance effects with both I$_3^-$ and I$_2$ species are to be expected and the spatial distribution of such components in the different UiO-67_NH$_2$(Zr,Hf) crystals were highlighted.

2. MATERIALS AND METHODS

2.1 SYNTHESES

The synthesis of the 2-amino-[1,1'-biphenyl]-4,4'-dicarboxylic acid (NH$_2$–H$_2$BPDC) is described in detail in the Supporting Information part (Figure S1).

UiO-67_NH$_2$(Zr) was typically prepared by a solvothermal treatment. In a 20 mL glass flask, zirconium chloride (ZrCl$_4$, Sigma Aldrich 99.9%, 100 mg, 0.429 mmol) was first dissolved in dimethylformamide (DMF, Sigma Aldrich, anhydrous 99.8%, 10 mL) under magnetic stirring for approximately 5 minutes. Then, NH$_2$–H$_2$BPDC linker ((COOH)$_2$C$_{12}$H$_7$NH$_2$, 220 mg, 0.855 mmol) was added to the solution, which was kept stirring for another 10 minutes. Finally, benzoic acid (C$_6$H$_5$COOH, Sigma Aldrich, ≥ 99.5%, 1.5 g, 0.12 mol) was added and the solution was maintained under stirring until complete dissolution of the precursors. The flask was placed inside an oven at 130 ºC for 48 h. After natural cooling, the crystals attached to the glass were gently pushed to the solution with the aid of a spatula. They were washed three times with fresh DMF (15 mL) and three times with fresh chloroform (CHCl$_3$, 15 mL Sigma Aldrich, ≥ 99.8%). The powder was activated under primary vacuum at 100 ºC for 1 h and finally, the solid was collected and kept in a flask under argon atmosphere.

UiO-67_NH$_2$(Hf) was solvothermally prepared as well. Hafnium chloride (HfCl$_4$, Sigma Aldrich 99.9%, 196 mg, 0.429 mmol), NH$_2$–H$_2$BPDC ((COOH)$_2$C$_{12}$H$_7$NH$_2$, 220 mg, 0.855 mmol), benzoic acid (C$_6$H$_5$COOH, Sigma Aldrich, $\geq$ 99.5%, 1.5 g, 0.12 mol) and dimethylformamide (DMF, Sigma Aldrich, anhydrous 99.8%, 10 mL) were initially added in a 20 mL glass flask following a procedure that is identical to that described above for UiO-67_NH$_2$(Zr). The collected solid was kept in a flask under argon atmosphere.

UiO-67_NH$_2$(Zr/Hf) followed the same synthesis procedure while respecting the molar desired Zr/Hf ratio. Shortly, the HfCl$_4$ and ZrCl$_4$ salts were pre-mixed in molar proportions of 1:1, based on a total 0.429 mmol for HfCl$_4$ + ZrCl$_4$. The molar ratio between the total amount of metal precursors and the other reactants was maintained constant.

2.2 STRUCTURAL CHARACTERIZATION

Inductively Coupled Plasma−Optical Emission Spectrometry: ICP−OES experiments were conducted using an Agilent 5110 ICP−OES spectrometer in the radial sighting mode. The mineralization of the samples was performed using 10 mg of the activated UiO-67_NH$_2$ compounds. First, the powdered samples were digested using a solution containing 10 mL of HF and 5 mL of HNO$_3$ and then they were heated to 140 °C for 48 h, followed by a dry evaporation step. Next, they were etched with aqua regia (HNO$_3$/HCl 3:6 mL), heated to 120 °C for 24 h, and dried to a residue of 0.5 mL. Finally, 9.5 mL of water was added, and the solution was diluted at 1/100 after filtration before being analysed using the 264.141 and 343.823 nm emission lines of hafnium and zirconium, respectively.

Single crystal X-ray diffraction: Single crystal X-ray diffraction experiments were done using a Bruker DUO-APEX2 diffractometer equipped with a two-dimensional CCD 4K detector and 2 m-sources generating Mo-Kα (λ = 0.71073 Å) and Cu-Kα (λ = 1.54178 Å) radiations. The structure refinement was conducted using the JANA software.

Surface area measurement: N_2 sorption was performed at liquid nitrogen temperature (77K) using a Micromeritics ASAP2020 apparatus using samples previously degassed under vacuum at 60 ºC. The specific surface area of the examined samples was evaluated by the multipoint BET (Brunauer–Emmett–Teller), in the range of pressure 0.015-0.30 P/P_0.

Scanning Electron Microscopy: SEM was conducted on a FEG microscope (Hitachi SU 5000) at an accelerating voltage of 5 kV, using samples previously sputter-coated with carbon. This microscope is equipped with a Si(Li) EDS detector (AZtec from the Oxford Instruments) with a 60 mm^2 window. For the EDS mapping the acceleration voltage was set to 10 kV.

Infrared spectroscopy: FTIR was performed on a Perkin Elmer Spectrum 2 spectrometer using an attenuated total reflectance (ATR) accessory and a diamond crystal as the reflective element. The spectra were recorded at a resolution of 4 cm^{-1} and 128 scans.

Raman spectroscopy: Micro-Raman Analyses were performed with a LabRam HR-Evolution (Horiba scientific) microspectrometer using a 50X 0.9 NA Olympus objective. The spectrometer is equipped with a 600 lines/mm grating. For excitation, 515 nm, 633 nm and 785 nm radiations were used. The Raman mapping was carried out using a spatial resolution of 1 μm. To evaluate only the thermodynamic aspect of the iodine distribution inside the pores (without any influence of kinetic phenomena) all the samples were kept sealed under argon atmosphere for one week after the contact with gaseous I_2. Also, to evaluate the kinetic of iodine diffusion, the spectra were collected in two different conditions: after 16 and 48 h of contact between the UiO-67_NH_2 solids and the iodine gas. Data processing and mapping analysis were performed using LabSpec6 software.

Bandgap evaluation: The apparent bandgap energy (E_g) of the materials was evaluated using the data obtained by diffuse reflectance UV-vis spectroscopy. E_g was assessed by plotting the so-called Kubelka-Munk

function [$(F(R)h\nu)^n$] against the photon energy ($h\nu$), where h is the Planck constant (4.14×10^{-15} eV.s), ν is the photon frequency (Hz), and F(R) is defined as below (Equation (1)). The index n is a function of the electron transition observed in the examined material – e.g., indirect allowed transition ($n = 1/2$), direct allowed transition ($n = 2$), indirect forbidden transition ($n = 3$), or direct forbidden transition ($n = 2/3$). F(R) was calculated by Equation (1), where R is the reflectance (%) assessed by UV-vis spectroscopy.

$$F(R) = \frac{(1 - R)^2}{2R} \qquad (1)$$

Nuclear magnetic resonance spectroscopy: Liquid ^1H NMR spectroscopy were performed in a Bruker AVANCE III HD 300 MHz spectrometer via a 60-position Sample Xpress autosampler. The chemical shifts were referenced by the external resonance of the tetramethylsilane. The sample digestion was performed using 10 mg of the UiO-67_NH$_2$ compounds. The material was soaked into 1 mL of a 4M NaOD/D$_2$O solution and sonicated for 15 minutes. Then, 0.6 mL of the liquid was recovered by filtration and placed into a 5 mm NMR tube before being analysed at 8 scans.

2.3 IODINE EVOLUTION TESTS

The gaseous iodine adsorption was conducted using a home-made filtration bench, previously described by Leloire et al. [6]. This setup allows for the collection of kinetic curves of iodine adsorption through a MOF powdered sample of approximately 30 mg during two days under room temperature.

The kinetics of adsorption for the different UiO-67_NH$_2$ materials were evaluated using the Linear Driving Force (LDF) model [19], which was already successfully applied in very similar systems containing UiO compounds and I$_2$ [6,8]. The LDF model is represented by Equation (2), where F(t) is the fractional uptake ($m_t . m_t$ $_{= 48h}$) – m_t is the uptake mass at a given time and $m_{t = 48h}$ is the uptake mass at $t = 48$ h, k_{LDF} is the effective

mass transfer coefficient (h^{-1}) at a given temperature and pressure (in this case, room temperature and ambient pressure), and t is the time in hours.

$$F(t) = 1 - e^{-k_{LDF}t} \tag{2}$$

3. RESULTS AND DISCUSSION

3.1 STRUCTURAL CHARACTERIZATION

In order to facilitate the comprehension of this manuscript, the textural and physical chemical properties of the UiO-67_NH$_2$(Zr,Hf) compounds are summarized in Table 1. In addition, a comparison between the structures of UiO-66_NH$_2$ and UiO-67_NH$_2$ is presented in Figure S2 to facilitate the comprehension and discussion of this manuscript.

Due to the relatively large and well-shaped octahedral crystal size (24 – 140 μm) obtained for the UiO-67_NH$_2$(Zr,Hf) compounds, single crystal XRD analysis was carried out for the three samples, for which diffraction intensities were collected after the activation procedure (Supporting Information). The positions and relative intensities of the diffraction Bragg peaks obtained from the single crystal XRD refinement for the UiO-67_NH$_2$(Zr,Hf) compounds are in good agreement with data from literature, with the observation of a typical cubic cell (space group Fm-$3m$, n°225), and a cell parameter of about 26.7 Å [20–22]. All three samples exhibited an important disorder related to the organic linker rotational movement along its axis, as verified by the shape of the elongated ellipsoids related to the aromatic carbons (Figure 1a). Moreover, the amino group also exhibited a great disorder associated due to the diffraction technique itself, which usually reveals the average positions of electronic densities in case of disordering configuration. In fact, the nitrogen atoms may have four equivalent positions because of the symmetry of the linker (2-amino, 3-amino, 2'-amino and 3'-amino) and therefore, they were refined considering an arbitrarily occupancy rate of 25% for each of these four possible sites (Figure 1b). On the other hand, it is not possible to distinguish the bridging μ$_3$–OH and μ$_3$–O positions (oxo and hydroxyl groups from the inorganic cluster that are connected to three M^{4+} cations, where

M = Zr or Hf) within the metallic hexameric $[M_6O_4(OH)_4]$ cluster because of their high cubic symmetry (*Fm-3m*), which creates an elongation on the ellipsoids (correlated to the hybrid OH and O group). Again, the refined sites for the μ_3–OH/O species are related to the average positions, considering that M–O bond distance will be shorter that the M–OH bond distances. Furthermore, the Zr/Hf ratio in the bimetallic UiO-67_NH$_2$(Zr/Hf) crystal (46%$_{at}$ of Zr and 54%$_{at}$ of Hf) was obtained through the refinement of the occupancy rate considering that both cations were located at a unique special position in the hexanuclear core.

The distances and the angles corresponding to the metal-oxygen bonds within the atomic arrangement of the structure are an important feature to be evaluated in these systems, as they were already ascribed to influence the iodine interaction with UiO-66(Zr,Hf) compounds [8]. The lattice parameter a was found to depend on the hafnium content, as the Zr^{4+} substitution by Hf^{4+} is sufficient to reduce it from 26.786(2) Å in UiO-67_NH$_2$(Zr), to 26.7376(6) Å and 26.723(2) Å in UiO-67_NH$_2$(Zr/Hf) and UiO-67_NH$_2$(Hf), respectively (Table S2). This decrease is in agreement with the behavior observed for a series of Zr/Hf-based UiO-66 compounds [8] and was ascribed to the shrinkage of the M–(OC) bond when passing from the UiO-66(Zr) (Zr–(OC) = 2.107(2) Å) [23] to the UiO-66(Hf) (Hf–(OC) = 2.086(8) Å) [24]. In fact, since Zr^{4+} and Hf^{4+} exhibit quite similar ionic radius (0.84 Å and 0.83 Å for Hf^{4+} and Zr^{4+}, respectively) concomitantly to a higher electronegativity of hafnium compared to that of zirconium (0.96 against 0.90), the Hf^{4+} is considered to present a higher Lewis acidity than the Zr^{4+} [25–30]. For such reason, the Hf^{4+} presence in UiO-66 samples induces a stiffening of the interatomic bond between the hexanuclear $[M_6O_4(OH)_4]$ core and the oxygen from carboxyl groups [24]. In the case of the UiO-67_NH$_2$(Zr,Hf) compounds, the occurrence of hafnium also reduces the M–(OC) bond length from 2.221(5) Å in UiO-67_NH$_2$(Zr), to 2.204(5) Å in UiO-67_NH$_2$(Zr/Hf), and to 2.206(9) Å in UiO-67_NH$_2$(Hf), as calculated from the single-crystal XRD refinement. This feature is coherent with the higher acid character of Hf^{4+}, as mentioned before [25–30].

In order to complement the textural properties of the UiO-67_NH$_2$(Zr,Hf) compounds, N$_2$ sorption experiments were conducted after the activation procedure (Figure 2). All the three samples exhibited a type-I isotherm according to the IUPAC classification, which is indicative of microporous materials [31]. Also, the

SSA values obtained for the compounds by applying the BET method are similar to other reports found in the literature [6], with 1329 ± 36, 1234 ± 34, and 914 ± 25 $m^2.g^{-1}$ for UiO-67_NH$_2$(Zr), UiO-67_NH$_2$(Zr/Hf) and UiO-67_NH$_2$(Hf), respectively. The related porous volumes are 0.68(4), 0.65(7) and 0.48(4) $cm^3.g^{-1}$, respectively. Moreover, the substitution of the zirconium by hafnium reduced the SSA values, which has already been reported in another work related to the UiO-66(Zr,Hf) series [8]. This decreasing behavior is consistent with the atomic weight of both considered elements (Zr = 91.224 $g.mol^{-1}$; Hf = 178.49 $g.mol^{-1}$), as the SSA is normalized by the mass of the material.

The crystal morphology of the UiO-67_NH$_2$ compounds was evaluated from SEM technique and is represented in Figure 3 alongside the EDS elemental mapping of the UiO-67_NH$_2$ samples. All the samples exhibit crystals with typical octahedral shape, which is expected for the UiO family [6,32]. It was observed that the crystal growth was favored in the bimetallic UiO-67_NH$_2$(Zr/Hf) sample, which exhibits the biggest crystal sizes ($\varnothing \approx 140$ μm) compared to both the UiO-67_NH$_2$(Hf) and UiO-67_NH$_2$(Zr) – $\varnothing \approx 44$ μm and $\varnothing \approx 51$ μm, respectively. Moreover, the triangular surfaces of the octahedra are smoother for the bimetallic UiO-67_NH$_2$(Zr/Hf), when compared to the other two samples. These features suggest that the amino group and the metal sites have a co-influence on the growth of UiO-67_NH$_2$ crystal. According to the work of Firth *et al.* [33] over the crystal growth of hafnium-based UiO-66, the organic linkers do not play an important role in the initial cluster formation; instead, they are involved latter in the reaction through post-cluster formation linker exchange. The framework growth with double cluster and even inter-cluster formation was ascribed to a transition from the **fcu** to a **hcp** unit [33]. Nevertheless, this was not the case in this work, as proven by SC-XRD. That being said, the improved growth of the crystals in the bimetallic UiO-67_NH$_2$(Zr/Hf) can be ascribed to a cooperative effect between the two metals and the rearrangement of the framework. In fact, Firth *et al.* [33] demonstrated that the crystalline framework grows alongside the linking of clusters together, suggesting that once they are linked, the dicarboxylate linkers are less labile and dissociation is kinetically and entropically less favorable. In other words, the co-presence of zirconium and hafnium must influence the dissociation of the NH$_2$–H$_2$BPDC linkers and their competition with the benzoic acid, slowing the reaction and consequentially, favoring the crystal growth. Furthermore, the distribution of zirconium, hafnium and

nitrogen in the crystals of the prepared compounds was evaluated through SEM technique and EDS elemental mapping (Figure 3). It is worth mentioning that shadow spots present in the bottom part of the images are due to the size of the crystals and to their relative position to the EDS detector, which reduces the intensity of the signal captured from these areas. Also, zirconium and hafnium elements are well distributed in the bimetallic UiO-67_NH$_2$, revealing that the UiO-67_NH$_2$(Zr/Hf) structure exhibits a homogeneous distribution of metals rather than two distinct families of crystal phases with an aggregation process (this would result in one phase with high hafnium content, and a second one with high zirconium content).

The vibrational modes of the synthesized UiO-67_NH$_2$(Zr,Hf) series were investigated by using FTIR and Raman spectroscopies (Figure 4) and are in agreement with other reports found in the literature [34,35]. Although no hydroxyl groups were revealed from the single-crystal XRD refinement (Supporting Information), the first FTIR absorption band, at 440 cm^{-1}, was ascribed to the asymmetric stretching of the μ_3–OH groups (which is basically the out-of-phase movement of the hydroxyl group connected to three metal cations) [20,34]. The absence of this contribution in the crystallographic structure is due to a limitation of the XRD technique, which is not able to thoroughly locate the position of hydrogen atoms from hydroxyl groups, present in the hexameric [(Zr,Hf)$_6$O$_4$(OH)$_4$] core, related to the UiO topology. Nevertheless, the occurrence of hydroxyl groups in the inorganic cluster was also confirmed by the FTIR absorption band around 710 cm^{-1} (Figure 4), which was ascribed to the μ_3–OH bending [20]. The other FTIR bands between 400 and 800 cm^{-1} were assigned to the inorganic vibrational modes (i.e., ν_{as}(M–(OC)) at 635 cm^{-1}, and ν(M–O) at 665 cm^{-1}) within the inorganic oxo-hydroxy hexanuclear cluster [20,34]. The bands related to the organic linker are visible starting from 700 cm^{-1}, worth mentioning the aromatic ring torsion mode at 770 cm^{-1}, the C–H bending at 1008 cm^{-1}, the C–O symmetric stretching at 1402 cm^{-1}, the C–O asymmetric stretching at 1595 cm^{-1}, and the C=C symmetric stretching at 1664 cm^{-1} [20,34]. Finally, the functionalization with the amino group was confirmed by the presence of the C–N stretching mode at 1275 cm^{-1}.

The Raman spectra were collected in order to obtain additional information about the vibrational modes of the UiO-67_NH$_2$(Zr,Hf) compounds. Up to 400 cm^{-1}, the Raman bands were attributed to hexameric polyoxo-

hydroxo core and/or lattice vibrations [20,24]. Then, between 400 and 700 cm^{-1}, bands related to the mixture of cluster and linker vibrations are observed [20,24]. The purely organic linker vibrations were found from 700 cm^{-1}, worth mentioning the bands at 846 cm^{-1} (C–C breathing mode) [24,35,36], at 1152 cm^{-1} (aromatic ring breathing mode) [24,35,36], at 1452 cm^{-1} (O–C–O symmetric stretching) [20,35], and at 1613 cm^{-1} (O–C–O asymmetric stretching) [20,35].

The UV-vis spectra were collected to evaluate the metal (Zr,Hf) influence over the electronic transitions and over the band gap energies of UiO-67_NH$_2$ materials (Figure 5). All the compounds exhibit broad absorption bands between 200 and 450 nm, with a tail that continues up to 600 nm. Based on EPR data and computational studies, Nasalevich *et al.* [37] demonstrated that its UiO-66_NH$_2$(Zr,Hf) parent presents a Linker-Based Transition (LBT), which is independent on its metal content (zirconium or hafnium). This feature was ascribed to the low binding energy of the empty d^0 orbitals of Zr^{4+} and Hf^{4+}, which inhibits the overlap with the π^* orbital of the NH$_2$–BDC linker, despite their geometric suitability [37]. Note that the main difference between UiO-66_NH$_2$ and UiO-67_NH$_2$ is the size of the linker, as the former has only one aromatic ring (NH$_2$–BDC) against two from the latter (NH$_2$–BPDC), and therefore, it is possible to infer that UiO-67_NH$_2$ also exhibits a LBT process. Furthermore, according to a computational study conducted by Yang *et al.* [38] over the UiO family, the partial density of states (PDOS) calculated for UiO-67(Zr) and UiO-67(Hf) reveals that both the Valence Band Maximum (VBM) and the Conduction Band Minimum (CBM) of UiO-67 are located on the organic linker (mostly *p*-orbitals of carbon and oxygen atoms) [38]. Finally, as already discussed by Yasin *et al.* [39], the presence of –NH$_2$ functions does not shift the positions of the VBM and CBM to the inorganic cluster. Instead, it adds mid-gap states that reduce the band gap energies without influencing their positions. Therefore, all these features converge to the same point, where it is assumed that both the VBM and the CBM of UiO-67_NH$_2$ are located on the NH$_2$–BPDC linker, regardless the metallic content of the MOF (zirconium and/or hafnium), similarly to what was observed for its UiO-66_NH$_2$ parent [39].

The band gap energies for UiO-67_NH$_2$(Zr,Hf) compounds were accessed through the Tauc plot of the Kubelka-Munk function [40–42]. According to the Tauc model, a material has a direct allowed transition (i.e., it

conserves the wave vector $\vec{k}$) if the plot of $(F(R)h\nu)^n$ against the photon energy ($h\nu$) exhibits a linear region when $n = 2$. Similarly, it exhibits an indirect band gap (i.e., it does not conserve the wave vector $\vec{k}$) if this region is present for $n = \frac{1}{2}$. However, in this case, both the considerations ($n = 2$ or $\frac{1}{2}$) result in a linear behavior around 3.0 eV, as shown in Figure 5. Moreover, Coulter and Birnie [43] demonstrated that some materials can present, simultaneously, direct and indirect band gaps, which would justify the acquisition of both E_g values. The $E_{g(dir)}$ was acquired by extrapolating the linear region of the $(F(R)h\nu)^2$ curve to the intercept with the abscissa axis, resulting in a $E_{g(dir)}$ value of 2.9 eV for UiO-67_NH2(Zr), UiO-67_NH2(Zr/Hf), and UiO-67_NH2 (Hf). However, when evaluating the indirect Tauc plot, one can observe that the curve has an initial inclination between 1.50 and 2.75 eV (Figure 5). Therefore, a baseline correction must be done in the $(F(R)h\nu)^{1/2}$ curve, as proposed by Makuła, Pacia, and Macyk [44]. In this case, the $E_{g(ind)}$ was obtained by extrapolating the linear region of the $(F(R)h\nu)^{1/2}$ curve until it intercepts the baseline of the data, resulting in a $E_{g(ind)}$ value of 2.8 eV for UiO-67_NH2(Zr), UiO-67_NH2 (Zr/Hf), and UiO-67_NH2 (Hf). When considering the Kubelka-Munk UV-Vis spectra, all the samples exhibits a linear region around 425 nm. In fact, it is only plausible to assume that the first electronic transition starting from lower to higher energies (higher to lower wavelengths) in the UV-vis spectra corresponds to the HOCO – LUCO transition in crystalline materials [37]. For this reason, it is possible to extrapolate the tangent line to the absorption band edge until it intercepts the abscissa axis and by transforming the wavelength to eV energies, find the E_g values for the materials. This interception occurs at 436, 429, and 426 nm – which corresponds to 2.84, 2.89, and 2.91 eV – for UiO-67_NH2(Zr), UiO-67_NH2(Zr/Hf), and UiO-67_NH2(Hf), respectively. Here, it is worth noticing that these results are in between the indirect and the direct band gaps and, although $E_{g(ind)} < E_{g(dir)}$, both of them are quite similar when comparing the same UiO-67_NH2 material (i.e., $E_{g(dir)\_UiO-67\_NH2(Zr)} = 2.9$ eV and $E_{g(ind)\_UiO-67\_NH2(Zr)} = 2.8$ eV), which justifies the acquisition of both values.

Finally, the presence of defects related to the missing of a NH2–BPDC linker was evaluated using liquid ^{1}H NMR spectroscopy (Figures S3, S4, S5, and S6). Actually, the benzoate (coming from the deprotonation of benzoic acid used as modulator in the syntheses process) is able to partially substitute the NH2–BPDC linker by generating defects of organic ditopic linkers. In fact, when an organic dicarboxylate linker is removed from

the UiO-67_NH$_2$ structure, it leaves the coordinating site with metallic centers (Zr or Hf) available for two monotopic benzoate molecules instead. Considering these two types of coordination modes (monotopic versus ditopic), if the molecular formula for the pristine UiO-67_NH$_2$ compound is represented by [M$_6$O$_4$(OH)$_4$L$_6$] (L = NH$_2$–BPDC), the absence of x ditopic linkers creates $2x$ carboxylate defects. Therefore, considering the presence of benzoate (B), the experimental molecular formula must be written as [M$_6$O$_4$(OH)$_4$(L)$_{6-x}$(B)$_{2x}$]. With that in mind, the integration of the NMR signal related to the benzoic acid was compared to that of the NH$_2$–BPDC linker for the three compounds, according to Equation (3).

$$\frac{2x}{6-x} = \frac{\int(B)}{\int(L)} \tag{3}$$

In light of this, the following chemical formulas were obtained considering the defects for each sample: UiO-67_NH$_2$(Zr) = [Zr$_6$O$_4$(OH)$_4$](L)$_{5.38}$(B)$_{1.24}$]; UiO-67_NH$_2$(Zr/Hf) = [Zr$_{2.76}$Hf$_{3.24}$O$_4$(OH)$_4$](L)$_{5.67}$(B)$_{0.66}$]; UiO-67_NH$_2$(Hf) = [Hf$_6$O$_4$(OH)$_4$](L)$_{5.52}$(B)$_{0.96}$]. Therefore, the UiO-67_NH$_2$(Zr), UiO-67_NH$_2$(Zr/Hf), and UiO-67_NH$_2$(Zr) compounds were found to exhibit 10.3, 5.5, and 8.0% of missing NH$_2$–BPDC linkers, respectively (Supporting Information). These results show that the number of defects in the samples are not directly connected to the hafnium content.

3.2 IODINE ADSORPTION WITHIN UiO-67_NH$_2$(Zr,Hf) FRAMEWORK

The iodine adsorption has been investigated in many MOF materials, for which the conversion of I$_2$ into I$_3^-$ has been often reported. Indeed, such a transformation was evaluated in few studies so far for UiO materials [6,8,45]. Also, other zirconium-based MOFs were found to present the same behavior when reducing the gaseous iodine molecules (MOF-808, NU-1000, MOF-867, UiO-66, and UiO-67) [45]. In some cases considering other metal sites, such as the nickel-based BOF-1, the electron transfer towards the I$_2$ molecules was ascribed to an oxidation of the metal sites, from Ni^{2+} into Ni^{3+} [15]. A similar feature was found for vanadium-based MOFs, where the oxidation of the V^{3+} centers were responsible for the production of I$_3^-$ [16]. However, this was proven

15

not to be the case in zirconium-based UiO-66 [6]. In fact, the mechanism for the I_2 reduction in UiO materials was only later proposed [8]. In this case, the I_2 reduction into I_3^- was attributed to an electron donor-acceptor (EDA) complex between the iodine molecule and the aromatic ring of the UiO linker [8]. This charge transfer complex between the linker and the iodine molecule was reported before in a MIL-53_NH_2 material, where the presence of high electron donor groups such as –NH_2 favored the I_2 adsorption by the MOF in a diluted cyclohexane solution [46]. One of the mainly used techniques to evaluate the presence of iodine is the Raman spectroscopy, as several species can be identified by characteristic bands in the $50 - 250$ cm^{-1} region [47–56]. Recently, three different contributions of iodine species were extracted using chemometric analysis of the Raman data in I_2@UiO-66(Zr,Hf) systems [8]. In this case, the band at 206 cm^{-1} was assigned to "free" I_2, which corresponds to gaseous iodine trapped within UiO pores presenting very weak interaction with its walls [54]. The bands at 173 and 156 cm^{-1}, attributed to "perturbed" I_2, include contributions of different iodine species whose spectral signature results from polyiodide I_n^- anions ($n = 5, 7, 9, ...$) [55,56]. These entities are progressively formed after adsorption from the reaction between the confined I_2 molecules and the MOFs walls. Finally, the two contributions at 115 and 141 cm^{-1} were ascribed to the symmetric and asymmetric I_3^- stretching modes, respectively [47,49,50,52,53,57,58]. The influence of the nature of the metal sites on the structure of UiO was demonstrated when zirconium was substituted by hafnium, resulting in a significant increase on the amount of iodine species trapped by the UiO framework [8,59]. Furthermore, it was demonstrated in a previous study that the I_2 to I_3^- conversion is improved by the smaller band gap of the UiO-66(Hf) material (4.0 against 4.1 eV for its zirconium parent), at the same time that the I_3^- stabilization was found to be favored by the presence of a higher acid metal site on the UiO structure (i.e., hafnium over zirconium) [8].

For better understanding of this behavior, the UiO-67_NH_2(Zr,Hf) samples were loaded with gaseous iodine following the same conditions as in previous studies – in contact with I_2 gas stream in a concentration of 0.08 mg.L^{-1} in argon, with a 10 L.h^{-1} flow rate, at room temperature [6,8]. A summary of the features observed after the iodine loading is presented in Table 2.

The adsorption kinetics evaluated by UV-vis for the different compounds is presented in Figure 6. The hafnium content has a clear influence over the amount of iodine captured by the material, where UiO-67_NH$_2$(Hf) exhibits the greatest capacity to retain I$_2$ (3428 g.mol^{-1} after 48 h of I$_2$ loading), followed by the mixed UiO-67_NH$_2$(Zr/Hf) (2835 g.mol^{-1} after 48 h of I$_2$ loading), and lastly by the UiO-67_NH$_2$(Zr) sample (1658 g.mol^{-1} after 48 h of I$_2$ loading). This tendency is in agreement with results obtained previously for I$_2$@UiO-66 compounds [8]. Indeed, the higher acidity of Hf^{4+} reduces the length of the M–(OC) bond from 2.221(5) Å in UiO-67_NH$_2$(Zr), to 2.206(9) Å in UiO-67_NH$_2$(Hf). As a result, the electron cloud of the NH$_2$–BPDC aromatic ring is delocalized towards the metal center, similar to what was observed in I$_2$@UiO-66(Hf,Zr) systems [8]. This effect enhances both I$_2$ uptake and I$_3^-$ formation as it improves the charge separation and reduces the electron-hole recombination. It is worth mentioning that the k_{LDF} and R^2 values for the bimetallic UiO-67_NH$_2$(Zr/Hf) are the smallest among all three samples, which should be related to the fact that this compound is the furthermost from reaching an adsorption plateau after 48 h of iodine adsorption (Figures 6 and S7). Here, it is worth reinforcing that the defects do not follow the same trend as observed for the I$_2$ adsorption capacity (i.e.: the zirconium-based compound exhibits more defects but less iodine uptake), implying that they did not have a considerable influence over the I$_2$ capture. Nevertheless, it seems that both the zirconium and hafnium-based UiO-67_NH$_2$ seemed to start arriving at a plateau after 48 h of adsorption, inferring that, contrary to the bimetallic sample, these compounds start to reach their maximum adsorption capacity. This effect might be related to a diffusion process of iodine through the UiO-67_NH$_2$ crystallites, which could be faster in the monometallic UiO-67_NH$_2$ samples. In fact, since the UiO-67_NH$_2$(Zr/Hf) crystals size are up to three times bigger than the monometallic samples, it is plausible that the diffusion process takes more time in this compound. Additionally, there is no direct correlation between the porous volumes of the UiO-67_NH$_2$(Zr,Hf) and the amounts of iodine trapped within the pores of the UiO-67 frameworks.

Seeking to understand the spatial distribution of the different iodine species, Raman mappings were conducted for the three UiO-67_NH$_2$(Zr,Hf) compounds using three distinct excitation wavelengths ($\lambda_1 = 515$ nm, $\lambda_2 = 633$ nm, and $\lambda_3 = 785$ nm) to take advantage of possible Raman resonance effect [54,60,61]. The laser wavelengths

have been chosen to correspond or not to the UV-vis absorption bands of the iodine species (Figure 7), aiming to enhance specific vibrations of these compounds. The adsorption of I_2 by the UiO-67_NH$_2$ samples gave rise to two bands maximizing at 290, and 350 nm, that were attributed to the formation of the anionic I_3^- species [62]. Other iodine forms may also be present in the spectra between 400 and 550 nm, resulting in a long adsorption tail towards the near-infrared region [8]. In fact, since the $\pi_g^* \rightarrow \sigma_u^*$ transitions related to the "isolated" iodine form in the gas phase (gaseous iodine without any interaction with the material) is expected to be found at about 520 nm [63,64], a signature assigned to the formation of a charge transfer complex between the I_2 and the NH$_2$–BPDC linker – which is a strong electron donor – is expected to be present at lower wavelengths (400 – 500 nm) [65,66].

It is worth mentioning that the charge transfer complex between the I_2 and the aromatic ring of the BDC linker was found to be favored by the smaller band gap of the hafnium-based samples in UiO-66 materials [8]. However, in the present work, the E_g values are not influenced by the metal site ($E_g^{ind} = 2.8$ eV, and $E_g^{dir} = 2.9$ eV), probably because of the presence of the amino group in the UiO-67_NH$_2$ linker. In fact, in the absence of the –NH$_2$ groups, the partial densities of states (PDOS) related to oxygen atoms in the valence band are influenced by the metal content of the sample and therefore, it can increase in energy in the presence of hafnium [38,39]. In contrast, when the –NH$_2$ group is considered, it creates a mid-gap state which virtually becomes the new valence band maximum, with no regard to the metal content [39]. For this reason, the E_g value is not a parameter to be considered here. Nevertheless, although UiO-67_NH$_2$(Hf) presents the same bandgap value as the other two samples, it demonstrated clearly higher iodine trapping capacity (3428 g.mol^{-1}) than UiO-67_NH$_2$(Zr/Hf) (2835 g.mol^{-1}) and, especially, than UiO-67_NH$_2$(Zr) (1658 g.mol^{-1}), as shown in Figure 6 and Table 1. This behavior suggests that other parameters than the bandgap values influence the I_2 adsorption and evolution processes.

At first, to obtain Raman spectra representative of the sample's composition, the excitation wavelength had to be chosen to avoid coupling with an electronic absorption of the iodine containing material. Therefore, considering the UV-vis spectra of the iodine loaded UiO-67_NH$_2$(Zr,Hf) materials presented in Figure 7, the

785 nm laser line that falls out of the absorption band was used to avoid Raman resonance effects and specific band intensity enhancement. Moreover, it is worth noting that Juang, Finzi and Bustamante [67] demonstrated that the penetration depth of the Raman laser increases with the wavelength source, which is the reason why the 785 nm laser is expected to penetrate deeper in the samples. The Raman mappings obtained in this non-resonance condition, after 16 h of I_2 contact, are displayed in Figure 8. Here, the zirconium-based UiO-67_NH$_2$ compound exhibited more I_2 and I_3^- species in the edges of the crystal than in its center. A similar feature was observed for the bimetallic UiO-67_NH$_2$(Zr/Hf) MOF, in which the iodine species are more concentrated in the edges of the crystal (red and brown regions). In contrast, after exposure of hafnium-based UiO-67_NH$_2$ to gaseous iodine, both I_2 and I_3^- species were homogeneously dispersed throughout the crystal. Here, it is worth mentioning that, after 16 h of exposure to iodine, the I_2 adsorption curves show that the maximum loading capacity is not reached whatever the metal content (Figure 6). However, the amount of iodine trapped by the hafnium sample is higher than that adsorbed by the bimetallic UiO-67_NH$_2$(Zr/Hf) and by the zirconium-based UiO-67_NH$_2$, regardless the duration of I_2 exposure. This validates the statement that replacing zirconium by hafnium in UiO compounds improves the kinetic of iodine adsorption [8,59]. It is important to mention that the differences in the Raman maps when comparing two different compounds (i.e.: the I_2 distribution in UiO-67_NH$_2$(Zr) and in UiO-67_NH$_2$(Hf) materials) are not related to the total amount of I_2 trapped by the MOF. In fact, the colors only evaluate the relative concentration of the species in the same crystal (i.e.: the colors cannot be compared between two different crystals). The presence of hafnium in UiO-67_NH$_2$ clearly improved the iodine access to the center of the crystal, as demonstrated by the higher homogeneity of both I_2 and I_3^- signals. On the other hand, a higher zirconium content is detrimental to the adsorption process, as zones of I_2 and I_3^- species are observed inhomogeneously in the crystals (Figure 8).

In order to verify if the same features are mantained for higher iodine loadings, Raman mappings were also conducted after 48 h of I_2 contact (Figure 9). In this case, the monometallic samples exhibited a more homogeneous distribution of both iodine species, whereas the bimetallic UiO-67_NH$_2$(Zr/Hf) still exhibits an heterogeneous distribution with the presence of multiple zones more or less concentrated in I_2 and I_3^-. When comparing the maps recorded at 16 and 48h, it is clear that the increase of the iodine loading is accompanied

by the I_2 and I_3^- migration to the center of the crystals, (Figures 8 and 9). However, this effect is not as marked in the bimetallic compound. This last point is probably related to the fact that UiO-67_NH$_2$(Zr/Hf) does not seem to reach its maximum adsorption capacity after 48 h, contrary to the monometallic compounds for which the maximum I_2 uptake seems close to being reached (Figure 6). This behavior highlights a combined effect between zirconium and hafnium in UiO-67_NH$_2$ when adsorbing iodine, as the bimetallic compound is the one that has the highest potential to improve its I_2 uptake in longer contact times.

Contrary to what has been found in previous studies for I_2@UiO-66 [8], the spectra obtained for all the I_2@UiO-67_NH$_2$(Zr,Hf) samples show only two contributions related to iodine: the first at around 170 cm^{-1} – related to "perturbed" I_2 –; and the second at 107 cm^{-1} – related to the symmetric stretching of I_3^- (Figure 8) [47–52]. It is worth mentioning that studies have reported the formation of polynuclear iodine species of I_n^- type ($n = 5$, 7, 9, …) after the charge transfer complex with organic donor molecules [55,56]. In fact, vibrations of I_5^- and I_7^- species were already observed around 170 cm^{-1} and contribute to the signal here named "perturbed" I_2 [52,58,68]. Note that, contrary to what was observed for UiO-66 compounds, the UiO-67_NH$_2$ materials seem to stabilize both "perturbed" I_2 and I_3^- species after the I_2 into I_3^- transformation reaches an equilibrium state (which happens a few weeks after the contact with the I_2 gas) [8]. This effect infers that UiO materials have a limited capacity to transform I_2 into I_3^-. Therefore, after reaching the maximum capacity of I_3^- transformation for greater iodine uptakes (which is the case for UiO-67_NH$_2$ compared to UiO-66), the new adsorbed I_2 do not transform into I_3^-. Instead, the molecules interact with the already formed I_3^- to produce the polyiodide I_n^- ($n = 5, 7, 9, …$) anions, which are then stabilized within the pores of the MOF. In addition, the fact that the band related to "free" I_2 (expected at about 210 cm^{-1}) is not present in UiO-67_NH$_2$(Zr,Hf) systems implies that the I_2 sorption and subsequent evolution into "perturbed" I_2 is already in an equilibrium state, as demonstrated elsewhere for UiO-66 compounds [8]. In UiO-66(Hf), the Raman band related to "free" I_2 vanishes 2 hours after leaving the iodine adsorption bench, whereas in UiO-66(Zr) this band is no longer observed after approximately 12 hours [8]. Finally, another interesting feature is the redshift observed in the "perturbed" I_2 and I_3^- vibrational modes: from 173 cm^{-1} in UiO-66(Zr,Hf) to 170 cm^{-1} in UiO-67_NH$_2$(Zr,Hf) for "perturbed" I_2; and from 115 to 107 cm^{-1} for I_3^-, respectively. This behavior highlights the influence of replacing the BDC by

the NH$_2$–BPDC linker in the interaction between the iodine molecule and the UiO-6X_Y (X = 6 or 7; Y = H or NH$_2$) compounds.

The Raman mappings were also recorded using the λ_{ex} = 633 nm excitation laser line seeking to assess possible specific band intensity enhancement by exciting in the tail of the absorption band of the iodine species (Figure 7). The mappings obtained after 16 h and 48 h of I$_2$ contact with the UiO-67_NH$_2$ materials are presented in Figures S8 and S9. The 2D spatial distributions are very similar to those obtained using the 785 nm excitation wavelength. After a 16-hour exposure to iodine, a homogeneous spatial distribution of the iodine species was observed for the hafnium-based UiO-67_NH$_2$, while the iodine species are concentrated in the edges of the crystal in the bimetallic UiO-67_NH$_2$(Zr/Hf), and in the monometallic UiO-67_NH$_2$(Zr), (Figure S8). On the other hand, for higher times of I$_2$ contact (48 h), both monometallic samples exhibited a homogeneous spatial distribution of I$_2$ and I$_3^-$ species, contrary to UiO-67_NH$_2$(Zr/Hf) which again presented a higher concentration of both signals in the edges of the crystal (Figure S8). This behavior agrees with that observed using the 785 nm excitation source, reinforcing the idea of a combined effect between Zr and Hf in UiO-67_NH$_2$, which shifts the adsorption maximum I$_2$ plateau to higher contact times (Figures 6, S8, and S9).

Finally, the Raman mappings were carried out using an excitation wavelength of 515 nm (Figure 10). This excitation source corresponds to the spectral region in which electronic transitions related to both I$_2$ and I$_3^-$ species are present, as observed in Figure 7 [62–66]. The coincidence between the wavelength of the excitation and that of the absorption bands is expected to enhance selectively the Raman bands intensities of the species involved in the electronic transition through Raman resonance effect. As observed using the 785 and 633 nm excitation laser lines, the difference in iodine concentration between the edges and the center of the crystal after 16h iodine loading was more marked when zirconium is present, but less pronounced in the bimetallic UiO-67_NH$_2$(Zr/Hf), and almost imperceptible in the UiO-67_NH$_2$(Hf) (Figure 10). However, after 48 h of iodine loading, in addition to the inhomogeneity of the two UiO-67_NH$_2$(Zr) and UiO-67_NH$_2$(Zr/Hf) samples, the hafnium-based compound also exhibited zones with different I$_2$ and I$_3^-$ concentrations, contrary to that observed for lower contact times (Figure 11).

21

It is worth mentioning that the change in the laser excitation source did not modify the positions of the I_2 and I_3^- bands, which were centered in the same wavenumbers for all three compounds: at 170 and 107 cm^{-1}, respectively. Nevertheless, the use of the 515 nm excitation wavelength was found to affect the relative intensities of the Raman bands characteristic of the iodine species (Figures 8, 9, 10, 11, S8, and S9). Indeed, while both the 785 and 633 nm spectra induce similar behavior with only weak differences when considering the relative areas of the bands at 107 cm^{-1} and 170 cm^{-1} ($[I_{170}/I_{107}]_{633,785nm} > 1$), this ratio is inversed for the Raman spectra collected at 515 nm ($[I_{170}/I_{107}]_{515nm} \approx 1$), for which the intensity of the 107 cm^{-1} line is significantly increased. This feature demonstrates the specific excitation of electronic transitions of the I_3^- species in resonance conditions (Figure 7) [60]. Indeed, the $\lambda_1 = 515$ nm excitation wavelength, which falls within the lower energy foot of the absorption band of the iodine species including I_3^- and adsorbed I_2 contributions (Figure 7), is assumed to induce more marked resonance effect for I_3^- [60]. This is equivalent to say that the I_3^- band will have a higher intensity in such conditions when compared to non-resonance circumstances [61]. This effect was less pronounced when using the $\lambda_2 = 633$ nm excitation wavelength, and negligible for the $\lambda_3 = 785$ nm laser (Figures 8, 9, 10, 11, S8, and S9), as those excitation sources fall out of the main absorption bands related to the iodine species (Figure 7).

When the excitation is performed using the 515 nm laser, the higher intensity enhancement of the I_3^- band compared to non-resonance conditions suggest higher I_3^- concentration. However, it is worth noting that the Raman resonance effect does not allow determination of the relative spectral concentration of the species (Figures 7, 10, and 11) [61]. Moreover, all the cartographies showed that the I_2 and the I_3^- species are concentrated nearby, which indicates that there is no considerable iodine diffusion after its transformation into I_3^- (Figures 8, 9, 10, 11, S8, and S9). The absence of I_3^- diffusion infers that the I_3^- has a stronger interaction with the UiO compounds than the I_2, which is in agreement with the results obtained for UiO-66 [8]. Indeed, in UiO-66(Zr,Hf) systems, it was proposed that the EDA complex between the BDC linker and the I_2 molecule generates a BDC$^{\bullet+}$ radical when reducing the I_2 into I_3^- [8]. The formation of this radical was ascribed to the absence of a redox phenomenon associated to the inorganic sites of UiO materials, as demonstrated in other

works [6,8,37]. The main reason for the absence of this metal reduction in zirconium and hafnium-based MOFs is the low binding energy (close to the vacuum level) of the d-orbitals from both Zr^{IV} and Hf^{IV} [37]. As a consequence, in I_2@UiO(Zr,Hf) systems, the I_2 reduction into I_3^- is purely related to the organic linker [8]. In fact, the EDA complex makes an electron to jump from the π^* orbital of the organic linker towards the σ^*_{5p} orbital of the I_2 molecule, leaving a hole (h^+) behind [8]. This entity was found to be stabilized through an electrostatic interaction between the recently formed I_3^- and the electron donor benzenedicarboxylate cation radical ($BDC^{\bullet+}$) [8]. However, in amino-functionalized NH_2–BDC materials – such as MIL-125_NH_2(Ti) – the hole created upon excitation was found to be stabilized by the –NH_2 group and by the carboxylate function of the linker, creating the corresponding $NH_2^{\bullet+}$–BDC radical [69]. Moreover, since organic linkers found in MIL-125_NH_2 and UiO-67_NH_2, have a similar benzene-derived structure (apart from having an extra aromatic ring), the –NH_2 groups should act as a hole stabilized in both cases [70]. Therefore, it is assumed that the corresponding $NH_2^{\bullet+}$–BPDC can also be formed in UiO-67_NH_2 systems. This feature supports the hypothesis that I_3^- has specific sites for adsorption, which are the places that stabilized the h^+ entity (aromatic ring, –NH_2, or –COO^-) [8,69–71]. Therefore, in this case, the main reason why the I_3^- has a lower diffusion capacity than I_2 is the electrostatic interaction that it creates with the generated holes in the UiO-67_NH_2 structure.

Aiming to deeper evaluate the iodine distribution in the biggest crystal with a considerable resolution, a Raman cartography was also conducted in three dimensions for the UiO-67_NH_2(Zr/Hf) compound for an adsorption time of 16h (Figure 12). In order to avoid the resonance effects with the iodine species and UiO-67_NH_2(Zr/Hf), the 785 nm laser was used as the excitation source. Here, the spatial distribution of the species characterized by the two regions related to "perturbed" I_2 (green) and I_3^- (blue) were evaluated up to 105 μm depth. As already demonstrated in the 2D Raman mappings using the 785 nm excitation source, the iodine species were mainly found at the edges of the bimetallic UiO-67_NH_2(Zr/Hf) compound. However, although the intensity of their contribution decreases with the depth (probably due to a loss of signal related to the laser probe in deeper distances and multi scattered phenomena) [72], the spatial distribution of "perturbed" I_2 and I_3^- is maintained, regardless the depth of the cartography.

With that in mind, one can conclude that several I_2 molecules did not reach the sites in the inner part of the crystals and therefore, they were not transformed into I_3^-, regardless its iodine exposure time (Figures 8, 9, 10, 11, 12, S8 and S9). This effect could be related to the faster kinetic of the I_2 into I_3^- transformation when compared to the diffusion rate of the species, probably because of the crystal size (which is three times bigger for the bimetallic compound). Indeed, if the kinetic of I_2 adsorption and evolution into I_3^- is faster than the species diffusion throughout the crystal, it is expected that both iodine species are concentrated in the edges rather than in the center as observed. Actually, it seems that the I_2 molecules are quickly attached to the NH_2–BPDC linkers, while the I_3^- anions are rapidly trapped by the respective $NH_2^{\bullet+}$–BPDC radicals right before their formation, which makes difficult their diffusion towards the center of the crystal. This behavior highlights the importance of tailoring not only the electronic structure and the functional groups of the MOFs when transforming iodine, but also their crystal size. In fact, in larger crystals, the diffusion process takes longer to reach the center of the structure, which can be detrimental if some of the transformed I_3^- molecules are trapped in their specific adsorption sites (aromatic ring, $-NH_2$, and $-COOH^-$) before reaching the center. This effect may not only reduce the mobility of this species, but also the number of available sites for new molecules to attach. Such behavior would also diminish the availability of locations for the EDA complex to take place. For instance, when considering the iodine trapped inside the UiO-67_NH_2(Zr,Hf) compounds, the transformation into I_3^- and its sub-sequential adsorption in specific sites can, at some point, obstruct some of the entrances to deeper pores inside the crystal structure, disturbing the iodine diffusion.

In this work, the iodine-loaded samples were stored during one to two weeks to guarantee a complete transformation of I_2 into I_3^- before the acquisition of the Raman maps. For such reason, they provide only direct information on the equilibrium state (when considering the I_2 evolution into I_3^-). Moreover, as already discussed above, there is no redox phenomena related to the Zr^{4+} and Hf^{4+} centers in UiO materials. Therefore, it is assumed that, similarly to what was found for the UiO-66 system [8], the electron transferred to the I_2 species comes from the EDA complex with the NH_2–BPDC linker. Then, the hole formed during the charge transfer must remain in the corresponding $NH_2^{\bullet+}$–BPDC radical, as mentioned before. At this point, due to electrostatic interactions, the I_3^- species should be chemically adsorbed on the $NH_2^{\bullet+}$–BPDC radical in UiO-

67_NH$_2$(Zr,Hf), which would also stabilize the h^+ entities in the framework [8]. Considering these features, it can be proposed that, after the NH$_2$–BPDC linker reduces one I$_2$ molecule, it loses its ability to transform other I$_2$ molecules into I$_3^-$ because of the electrostatic repulsion created by the presence of two holes in the same linker [73–75]. This behavior is coherent with the results obtained for the UiO-67_NH$_2$ compounds in this work as, even though there are still I$_2$ molecules available to be transformed in the pores, the transformation of I$_2$ into I$_3^-$ in UiO-67_NH$_2$ systems reaches an equilibrium after a few days, regardless of the iodine loading. Indeed, since the UiO-67_NH$_2$ materials adsorbed up to 6 times more iodine than their UiO-66 parents after 16 h of I$_2$ contact (2419 against 285 g.mol^{-1} for UiO-67_NH$_2$(Hf) and UiO-66(Hf), respectively), lots of untransformed I$_2$ molecules were trapped inside the pores – even after one week. This feature was ascribed to the bigger pores of UiO-67_NH$_2$(Zr,Hf) materials (21.5 Å against 6.4 Å in UiO-66_NH$_2$) [76,77], which can accommodate more I$_2$ molecules (even though, at this point, the NH$_2$–BPDC linkers have reduced ability to transform them into I$_3^-$). Moreover, the effect related to the presence of the amino group is also to be considered because –NH$_2$ is known to favor the I$_3^-$ formation, as highlighted in other works [6,13,46]. Actually, functions with high electron donor character can induce the polarization of the electronic cloud of the iodine molecule [46], improving the EDA complex between the linker and the I$_2$ molecule, which produces a faster I$_2$ into I$_3^-$ transformation [6,8]. This behavior results in a "perturbed" I$_2$ signal much more intense than that of I$_3^-$ in non-resonance conditions for all the UiO-67_NH$_2$(Zr,Hf) samples (Figures 8, 10, and S8). Finally, in order to better understand the influence of the metal sites and of the resonance phenomenon on the stabilization and semi-quantification of the iodine species, the ratio between the areas of the I$_2$ and I$_3^-$ signals were plotted according to the laser wavelength (Figure S10). This figure demonstrates that the [A_{170}/A_{107}] ratio increases gradually with the laser wavelength and that the resonance effect is more pronounced for the I$_3^-$ vibrational mode, as the λ_{ex} = 515 nm laser generates the lower [A_{170}/A_{107}] signal (due to an increase in the A_{107} signal).

4. CONCLUSIONS

Three UiO-67_NH$_2$ samples with different metal contents (Zr, Zr/Hf and Hf) were successfully synthesized and loaded with gaseous iodine. The hafnium-based UiO-67_NH$_2$ achieved the best retaining capacity after

48 h of I_2 contact, capturing 3428 g.mol^{-1} of iodine, followed by the mixed UiO-67_NH$_2$(Zr/Hf) with 2835 g.mol^{-1} and then by the zirconium-based UiO-67_NH$_2$, with 1658 g.mol^{-1}. Nevertheless, the bimetallic compound did not seem to reach a plateau regarding the I_2 adsorption, which infers that it may surpass the hafnium-based compound in contact times higher than 48 h. This feature was related to the size of its crystals, which are about three times bigger than the monometallic compounds and can attenuate the diffusion of the I_2 species. Moreover, a I_2 into I_3^- conversion was verified in the pores of the crystals after the contact with the gaseous flow as highlighted by Raman spectroscopy through the presence of bands related to "perturbed" I_2 (at about 170 cm^{-1}) and I_3^- (at about 107 cm^{-1}). Three laser excitation sources were used for evaluating the spatial distribution of the species: 515, 633, and 785 nm. A Raman resonance effect with the I_3^- species was observed with the 515 nm excitation wavelength, but it was less noticeable for the 633 nm laser and absent with the 785 nm source. Also, the Raman mapping for low contact times (16 h) demonstrated that the UiO-67_NH$_2$(Hf) displayed the most homogeneous distribution of both the I_2 and I_3^- species among the three compounds, whereas the zirconium-based and the bimetallic UiO-67_NH$_2$ exhibited zones with different concentrations of such iodine species. However, for higher contact times (48 h), only the UiO-67_NH$_2$(Zr/Hf) material exhibited an inhomogeneous spatial distribution of the iodine species, which was related to the fact that the I_2 capture did not reach its maximum adsorption plateau in this case. Additionally, the spatial distribution of the iodine species revealed that I_3^- does not diffuse after its formation, reason why the regions with more I_2 are also fulfilled with I_3^-. This effect was associated to the presence of specific adsorption sites for the I_3^- anions, as proposed before in other study using UiO-66(Zr,Hf) [8]. In fact, in UiO-67_NH$_2$(Zr,Hf) systems, the cation radical NH$_2^{\bullet+}$–BPDC (analogous to the BDC$^{\bullet+}$ for UiO-66 materials) was ascribed to be the center for the specific adsorption of I_3^- anions. This feature indicates that there is a maximum amount of I_3^- that can be trapped in UiO materials before it gets saturated, which is intrinsically related to the hole-hole Coulomb repulsions in the organic linker radical [73–75]. This study increases the comprehension of the iodine evolution mechanism as it reinforces the stronger interaction between the anionic I_3^- species and the MOFs lattice when compared to that of the I_2 molecules. Further studies must be conducted in order to evaluate the stability of I_3^- species in different conditions such as temperature and humidity.

5. SUPPORTING INFORMATION

NH$_2$–BPDC syntheses protocols, crystallographic data, ^{1}H NMR spectra, LDF model regression, and Raman mapping data.

6. ACKNOWLEDGMENTS

6. REFERENCES

(1)   Zablotska, L. B. 30 Years After the Chernobyl Nuclear Accident: Time for Reflection and Re-Evaluation of Current Disaster Preparedness Plans. *J. Urban Heal.* **2016**, *93* (3), 407–413. https://doi.org/10.1007/s11524-016-0053-x.

(2)   Lin, W.; Chen, L.; Yu, W.; Ma, H.; Zeng, Z.; Lin, J.; Zeng, S. Radioactivity Impacts of the Fukushima Nuclear Accident on the Atmosphere. *Atmos. Environ.* **2015**, *102*, 311–322. https://doi.org/10.1016/j.atmosenv.2014.11.047.

(3)   Riley, B. J.; Vienna, J. D.; Strachan, D. M.; McCloy, J. S.; Jerden, J. L. Materials and Processes for the Effective Capture and Immobilization of Radioiodine: A Review. *Journal of Nuclear Materials*. 2016, pp 307–326. https://doi.org/10.1016/j.jnucmat.2015.11.038.

(4)   Pesce, L.; Kopp, P. Iodide Transport: Implications for Health and Disease. *Int. J. Pediatr. Endocrinol.* **2014**, *2014* (1), 1–12. https://doi.org/10.1186/1687-9856-2014-8.

(5)   Xie, W.; Cui, D.; Zhang, S. R.; Xu, Y. H.; Jiang, D. L. Iodine Capture in Porous Organic Polymers and Metal-Organic Frameworks Materials. *Mater. Horizons* **2019**, *6* (8), 1571–1595. https://doi.org/10.1039/c8mh01656a.

(6)   Leloire, M.; Walshe, C.; Devaux, P.; Giovine, R.; Duval, S.; Bousquet, T.; Chibani, S.; Paul, J.; Moissette, A.; Vezin, H.; Nerisson, P.; Cantrel, L.; Volkringer, C.; Loiseau, T. Capture of Gaseous Iodine in Isoreticular Zirconium-Based UiO-n Metal-Organic Frameworks: Influence of Amino Functionalization, DFT Calculations, Raman and EPR Spectroscopic Investigation. *Chem. – A Eur. J.* **2022**, *28* (14), e202104437. https://doi.org/10.1002/chem.202104437.

(7)   Leloire, M.; Dhainaut, J.; Devaux, P.; Leroy, O.; Desjonqueres, H.; Poirier, S.; Nerisson, P.; Cantrel, L.; Royer, S.; Loiseau, T.; Volkringer, C. Stability and Radioactive Gaseous Iodine-131 Retention Capacity of Binderless UiO-66-NH2 Granules under Severe Nuclear Accidental Conditions. *J. Hazard. Mater.* **2021**, *416*, 125890. https://doi.org/10.1016/j.jhazmat.2021.125890.

(8)   Andrade, P. H. M.; Henry, N.; Volkringer, C.; Loiseau, T.; Vezin, H.; Hureau, M.; Moissette, A. Iodine Uptake by Zr-/Hf-Based UiO-66 Materials: The Influence of Metal Substitution on Iodine

Evolution. *ACS Appl. Mater. Interfaces* **2022**. https://doi.org/10.1021/acsami.2c07288.

(9) Assaad, T.; Assfour, B. Metal Organic Framework MIL-101 for Radioiodine Capture and Storage. *J. Nucl. Mater.* **2017**, *493*, 6–11. https://doi.org/10.1016/j.jnucmat.2017.05.036.

(10) Khan, N. A.; Hasan, Z.; Jhung, S. H. Adsorptive Removal of Hazardous Materials Using Metal-Organic Frameworks (MOFs): A Review. *J. Hazard. Mater.* **2013**, *244–245*, 444–456. https://doi.org/10.1016/j.jhazmat.2012.11.011.

(11) Zhang, X.; Maddock, J.; Nenoff, T. M.; Denecke, M. A.; Yang, S.; Schröder, M. Adsorption of Iodine in Metal-Organic Framework Materials. *Chem. Soc. Rev.* **2022**, 3243–3262. https://doi.org/10.1039/d0cs01192d.

(12) Marshall, R. J.; Griffin, S. L.; Wilson, C.; Forgan, R. S. Stereoselective Halogenation of Integral Unsaturated C-C Bonds in Chemically and Mechanically Robust Zr and Hf MOFs. *Chem. – A Eur. J.* **2016**, *22* (14), 4870–4877. https://doi.org/10.1002/chem.201505185.

(13) Lee, B.; Park, J. Effect of Functional Groups on the I2 Sorption Kinetics of Isostructural Metal–Organic Frameworks. *Bull. Korean Chem. Soc.* **2021**, *42* (2), 290–293. https://doi.org/10.1002/bkcs.12201.

(14) Brunet, G.; Safin, D. A.; Aghaji, M. Z.; Robeyns, K.; Korobkov, I.; Woo, T. K.; Murugesu, M. Stepwise Crystallographic Visualization of Dynamic Guest Binding in a Nanoporous Framework. *Chem. Sci.* **2017**, *8* (4), 3171–3177. https://doi.org/10.1039/C7SC00267J.

(15) Hye, J. C.; Myunghyun, P. S. Dynamic and Redox Active Pillared Bilayer Open Framework: Single-Crystal-to-Single-Crystal Transformations upon Guest Removal, Guest Exchange, and Framework Oxidation. *J. Am. Chem. Soc.* **2004**, *126* (48), 15844–15851. https://doi.org/10.1021/ja0466715.

(16) Zhang, X.; Da Silva, I.; Fazzi, R.; Sheveleva, A. M.; Han, X.; Spencer, B. F.; Sapchenko, S. A.; Tuna, F.; McInnes, E. J. L.; Li, M.; Yang, S.; Schröder, M. Iodine Adsorption in a Redox-Active Metal-Organic Framework: Electrical Conductivity Induced by Host-Guest Charge-Transfer. *Inorg. Chem.* **2019**, *58* (20), 14145–14150. https://doi.org/10.1021/acs.inorgchem.9b02176.

(17) Kostański, L. K.; Króalikowski, W. Bulk Polymerization of Diallyl Benzene-Dicarboxylates I. Influence of Temperature on Allyl Group Reactivity. *J. Polym. Sci. Polym. Chem. Ed.* **1985**, *23* (3),

605–614. https://doi.org/10.1002/pol.1985.170230302.

(18)   Attygalle, A. B.; Chan, C.-C.; Axe, F. U.; Bolgar, M. Generation of Gas-Phase Sodiated Arenes Such as [(Na3(C6H4)+] from Benzene Dicarboxylate Salts. *J. Mass Spectrom.* **2010**, *45* (1), 72–81. https://doi.org/10.1002/jms.1690.

(19)   Sircar, S.; Hufton, J. R. Why Does the Linear Driving Force Model for Adsorption Kinetics Work? *Adsorption* **2000**, *6* (2), 137–147. https://doi.org/10.1023/A:1008965317983.

(20)   Chavan, S.; Vitillo, J. G.; Gianolio, D.; Zavorotynska, O.; Civalleri, B.; Jakobsen, S.; Nilsen, M. H.; Valenzano, L.; Lamberti, C.; Lillerud, K. P.; Bordiga, S. H2 Storage in Isostructural UiO-67 and UiO-66 MOFs. *Phys. Chem. Chem. Phys.* **2012**, *14* (5), 1614–1626. https://doi.org/10.1039/c1cp23434j.

(21)   Marshall, R. J.; Hobday, C. L.; Murphie, C. F.; Griffin, S. L.; Morrison, C. A.; Moggach, S. A.; Forgan, R. S. Amino Acids as Highly Efficient Modulators for Single Crystals of Zirconium and Hafnium Metal-Organic Frameworks. *J. Mater. Chem. A* **2016**, *4* (18), 6955–6963. https://doi.org/10.1039/c5ta10401g.

(22)   Kaposi, M.; Cokoja, M.; Hutterer, C. H.; Hauser, S. A.; Kaposi, T.; Klappenberger, F.; Pöthig, A.; Barth, J. V; Herrmann, W. A.; Kühn, F. E. Immobilisation of a Molecular Epoxidation Catalyst on UiO-66 and -67: The Effect of Pore Size on Catalyst Activity and Recycling. *Dalt. Trans.* **2015**, *44* (36), 15976–15983. https://doi.org/10.1039/C5DT01340B.

(23)   Cavka, J. H.; Jakobsen, S.; Olsbye, U.; Guillou, N.; Lamberti, C.; Bordiga, S.; Lillerud, K. P. A New Zirconium Inorganic Building Brick Forming Metal Organic Frameworks with Exceptional Stability. *J. Am. Chem. Soc.* **2008**, *130* (42), 13850–13851. https://doi.org/10.1021/ja8057953.

(24)   Valenzano, L.; Civalleri, B.; Chavan, S.; Bordiga, S.; Nilsen, M. H.; Jakobsen, S.; Lillerud, K. P.; Lamberti, C. Disclosing the Complex Structure of UiO-66 Metal Organic Framework: A Synergic Combination of Experiment and Theory. *Chem. Mater.* **2011**, *23* (7), 1700–1718. https://doi.org/10.1021/cm1022882.

(25)   Shannon, R. D. Revised Effective Ionic Radii and Systematic Studies of Interatomic Distances in Halides and Chalcogenides. *Acta Crystallogr. Sect. A Cryst. physics, diffraction, Theor. Gen. Crystallogr.* **1976**, *32* (5), 751–767. https://doi.org/10.1107/S0567739476001551.

(26) Islamoglu, T.; Ray, D.; Li, P.; Majewski, M. B.; Akpinar, I.; Zhang, X.; Cramer, C. J.; Gagliardi, L.; Farha, O. K. From Transition Metals to Lanthanides to Actinides: Metal-Mediated Tuning of Electronic Properties of Isostructural Metal-Organic Frameworks. *Inorg. Chem.* **2018**, *57* (21), 13246–13251. https://doi.org/10.1021/acs.inorgchem.8b01748.

(27) Jeong, N. C.; Lee, J. S.; Tae, E. L.; Lee, Y. J.; Yoon, K. B. Acidity Scale for Metal Oxides and Sanderson's Electronegativities of Lanthanide Elements. *Angew. Chemie - Int. Ed.* **2008**, *47* (52), 10128–10132. https://doi.org/10.1002/anie.200803837.

(28) Hadjiivanov, K. I.; Panayotov, D. A.; Mihaylov, M. Y.; Ivanova, E. Z.; Chakarova, K. K.; Andonova, S. M.; Drenchev, N. L. Power of Infrared and Raman Spectroscopies to Characterize Metal-Organic Frameworks and Investigate Their Interaction with Guest Molecules. *Chem. Rev.* **2021**, *121* (3), 1286–1424. https://doi.org/10.1021/acs.chemrev.0c00487.

(29) Klet, R. C.; Liu, Y.; Wang, T. C.; Hupp, J. T.; Farha, O. K. Evaluation of Brønsted Acidity and Proton Topology in Zr- and Hf-Based Metal-Organic Frameworks Using Potentiometric Acid-Base Titration. *J. Mater. Chem. A* **2016**, *4* (4), 1479–1485. https://doi.org/10.1039/c5ta07687k.

(30) Bakuru, V. R.; Churipard, S. R.; Maradur, S. P.; Kalidindi, S. B. Exploring the Brønsted Acidity of UiO-66 (Zr, Ce, Hf) Metal–Organic Frameworks for Efficient Solketal Synthesis from Glycerol Acetalization. *Dalt. Trans.* **2019**, *48* (3), 843–847. https://doi.org/10.1039/c8dt03512a.

(31) Sing, K. S. W. Reporting Physisorption Data for Gas/Solid Systems with Special Reference to the Determination of Surface Area and Porosity. *Pure Appl. Chem.* **1982**, *54* (11), 2201–2218. https://doi.org/10.1351/pac198557040603.

(32) Schaate, A.; Roy, P.; Godt, A.; Lippke, J.; Waltz, F.; Wiebcke, M.; Behrens, P. Modulated Synthesis of Zr-Based Metal-Organic Frameworks: From Nano to Single Crystals. *Chem. - A Eur. J.* **2011**, *17* (24), 6643–6651. https://doi.org/10.1002/chem.201003211.

(33) Firth, F. C. N.; Gaultois, M. W.; Wu, Y.; Stratford, J. M.; Keeble, D. S.; Grey, C. P.; Cliffe, M. J. Exploring the Role of Cluster Formation in UiO Family Hf Metal-Organic Frameworks with in Situ X-Ray Pair Distribution Function Analysis. *J. Am. Chem. Soc.* **2021**, *143* (47), 19668–19683. https://doi.org/10.1021/jacs.1c06990.

(34) Goodenough, I.; Devulapalli, V. S. D.; Xu, W.; Boyanich, M. C.; Luo, T. Y.; De Souza, M.; Richard, M.; Rosi, N. L.; Borguet, E. Interplay between Intrinsic Thermal Stability and Expansion Properties of Functionalized UiO-67 Metal-Organic Frameworks. *Chem. Mater.* **2021**, *33* (3), 910–920. https://doi.org/10.1021/acs.chemmater.0c03889.

(35) Sen Bishwas, M.; Malik, M.; Poddar, P. Raman Spectroscopy-Based Sensitive, Fast and Reversible Vapour Phase Detection of Explosives Adsorbed on Metal-Organic Frameworks UiO-67. *New J. Chem.* **2021**, *45* (16), 7145–7153. https://doi.org/10.1039/d0nj04915h.

(36) Shearer, G. C.; Chavan, S.; Ethiraj, J.; Vitillo, J. G.; Svelle, S.; Olsbye, U.; Lamberti, C.; Bordiga, S.; Lillerud, K. P. Tuned to Perfection: Ironing out the Defects in Metal-Organic Framework UiO-66. *Chem. Mater.* **2014**, *26* (14), 4068–4071. https://doi.org/10.1021/cm501859p.

(37) Nasalevich, M. A.; Hendon, C. H.; Santaclara, J. G.; Svane, K.; Van Der Linden, B.; Veber, S. L.; Fedin, M. V.; Houtepen, A. J.; Van Der Veen, M. A.; Kapteijn, F.; Walsh, A.; Gascon, J. Electronic Origins of Photocatalytic Activity in D0 Metal Organic Frameworks. *Sci. Rep.* **2016**, *6* (November 2015), 1–9. https://doi.org/10.1038/srep23676.

(38) Yang, L. M.; Ganz, E.; Svelle, S.; Tilset, M. Computational Exploration of Newly Synthesized Zirconium Metal-Organic Frameworks UiO-66, -67, -68 and Analogues. *J. Mater. Chem. C* **2014**, *2* (34), 7111–7125. https://doi.org/10.1039/c4tc00902a.

(39) Yasin, A. S.; Li, J.; Wu, N.; Musho, T. Study of the Inorganic Substitution in a Functionalized UiO-66 Metal-Organic Framework. *Phys. Chem. Chem. Phys.* **2016**, *18* (18), 12748–12754. https://doi.org/10.1039/c5cp08070c.

(40) Kubelka, P.; Munk, F. An Article on Optics of Paint Layers. *Z. Tech. Phys.* **1931**, *12* (1930), 593–601.

(41) Tauc, J. Optical Properties and Electronic Structure of Amorphous Ge and Si. *Mater. Res. Bull.* **1968**, *3* (1), 37–46. https://doi.org/10.1016/0025-5408(68)90023-8.

(42) Tauc, J.; Grigorovici, R.; Vancu, A. Optical Properties and Electronic Structure of Amorphous Germanium. *Phys. status solidi* **1966**, *15* (2), 627–637. https://doi.org/10.1002/pssb.19660150224.

(43) Coulter, J. B.; Birnie, D. P. Assessing Tauc Plot Slope Quantification: ZnO Thin Films as a Model

System. *Phys. Status Solidi Basic Res.* **2018**, *255* (3), 1–7. https://doi.org/10.1002/pssb.201700393.

(44)   Makuła, P.; Pacia, M.; Macyk, W. How To Correctly Determine the Band Gap Energy of Modified Semiconductor Photocatalysts Based on UV-Vis Spectra. *J. Phys. Chem. Lett.* **2018**, *9* (23), 6814–6817. https://doi.org/10.1021/acs.jpclett.8b02892.

(45)   Chen, P.; He, X.; Pang, M.; Dong, X.; Zhao, S.; Zhang, W. Iodine Capture Using Zr-Based Metal-Organic Frameworks (Zr-MOFs): Adsorption Performance and Mechanism. *ACS Appl. Mater. Interfaces* **2020**, *12* (18), 20429–20439. https://doi.org/10.1021/acsami.0c02129.

(46)   Falaise, C.; Volkringer, C.; Facqueur, J.; Bousquet, T.; Gasnot, L.; Loiseau, T. Capture of Iodine in Highly Stable Metal-Organic Frameworks: A Systematic Study. *Chem. Commun.* **2013**, *49* (87), 10320–10322. https://doi.org/10.1039/c3cc43728k.

(47)   Deplano, P.; Devillanova, F. A.; Ferraro, J. R.; Isaia, F.; Lippolis, V.; Mercuri, M. L. On the Use of Raman Spectroscopy in the Characterization of Iodine in Charge-Transfer Complexes. *Appl. Spectrosc.* **1992**, *46* (11), 1625–1629.

(48)   Cooney, R. P.; Hendra, P. J.; Fleischmann, M. Raman Spectra from Adsorbed Iodine Species on an Unroughened Platinum Electrode Surface. *J. Raman Spectrosc.* **1977**, *6* (5), 264–266. https://doi.org/10.1002/jrs.1250060510.

(49)   Deplano, P.; Ferraro, J. R.; Mercuri, M. L.; Trogu, E. F. Structural and Raman Spectroscopic Studies as Complementary Tools in Elucidating the Nature of the Bonding in Polyiodides and in Donor-I2 Adducts. *Coord. Chem. Rev.* **1999**, *188* (1), 71–95. https://doi.org/10.1016/S0010-8545(98)00238-0.

(50)   Svensson, P. H.; Kloo, L. Synthesis, Structure, and Bonding in Polyiodide and Metal Iodide-Iodine Systems. *Chem. Rev.* **2003**, *103* (5), 1649–1684. https://doi.org/10.1021/cr0204101.

(51)   Wang, C.; Wang, Y.; Ge, R.; Song, X.; Xing, X.; Jiang, Q.; Lu, H.; Hao, C.; Guo, X.; Gao, Y.; Jiang, D. A 3D Covalent Organic Framework with Exceptionally High Iodine Capture Capability. *Chem. – A Eur. J.* **2018**, *24* (3), 585–589. https://doi.org/10.1002/chem.201705405.

(52)   Zhang, W.; Mu, Y.; He, X.; Chen, P.; Zhao, S.; Huang, C.; Wang, Y.; Chen, J. Robust Porous Polymers Bearing Phosphine Oxide/Chalcogenide Ligands for Volatile Iodine Capture. *Chem. Eng. J.* **2020**, *379* (June 2019), 122365. https://doi.org/10.1016/j.cej.2019.122365.

(53)   Hsu, S. L.; Signorelli, A. J.; Pez, G. P.; Baughman, R. H. Highly Conducting Iodine Derivatives of Polyacetylene: Raman, XPS and X-ray Diffraction Studies. *J. Chem. Phys.* **1978**, *69* (1), 106–111. https://doi.org/10.1063/1.436393.

(54)   Kiefer, W.; Bernstein, H. J. Resonance Raman Spectroscopic Study on Iodine in Various Organic Solvents: Spectroscopic Constants and Halfband Widths of the I2 Vibration. *J. Raman Spectrosc.* **1973**, *1* (5), 417–431. https://doi.org/10.1002/jrs.1250010502.

(55)   Klaeboe, P. The Raman Spectra of Some Iodine, Bromine, and Iodine Monochloride Charge-Transfer Coomplexes in Solution. *J. Am. Chem. Soc.* **1967**, *89* (15), 3667–3676. https://doi.org/10.1021/ja00991a001.

(56)   Lobanov, S. S.; Daly, J. A.; Goncharov, A. F.; Chan, X.; Ghose, S. K.; Zhong, H.; Ehm, L.; Kim, T.; Parise, J. B. Iodine in Metal-Organic Frameworks at High Pressure. *J. Phys. Chem. A* **2018**, *122* (29), 6109–6117. https://doi.org/10.1021/acs.jpca.8b05443.

(57)   Cooney, R. P.; Hendra, P. J.; Fleischmann, M. Raman Spectra from Adsorbed Iodine Species on an Unroughened Platinum Electrode Surface. *J. Raman Spectrosc.* **1977**, *6* (5), 264–266. https://doi.org/10.1002/jrs.1250060510.

(58)   Wang, C.; Wang, Y.; Ge, R.; Song, X.; Xing, X.; Jiang, Q.; Lu, H.; Hao, C.; Guo, X.; Gao, Y.; Jiang, D. A 3D Covalent Organic Framework with Exceptionally High Iodine Capture Capability. *Chem. – A Eur. J.* **2018**, *24* (3), 585–589. https://doi.org/10.1002/chem.201705405.

(59)   Guan, Y.; Li, Y.; Zhou, J.; Zhang, T.; Ding, J.; Xie, Z.; Wang, L. Defect Engineering of Nanoscale Hf-Based Metal–Organic Frameworks for Highly Efficient Iodine Capture. *Inorg. Chem.* **2021**. https://doi.org/10.1021/acs.inorgchem.1c01120.

(60)   Nour, E. M.; Chen, L. H.; Laane, J. Resonance Raman and Far-infrared Studies of Charge-transfer Complexes of Iodine. *J. Raman Spectrosc.* **1986**, *17* (6), 467–469. https://doi.org/10.1002/jrs.1250170608.

(61)   Strommen, D. P.; Nakamoto, K. Resonance Raman Spectroscopy. *J. Chem. Educ.* **1977**, *54* (8), 474. https://doi.org/10.1021/ed054p474.

(62)   Gardner, J. M.; Abrahamsson, M.; Farnum, B. H.; Meyer, G. J. Visible Light Generation of Iodine

Atoms and I-I Bonds: Sensitized I- Oxidation and I3 - Photodissociation. *J. Am. Chem. Soc.* **2009**, *131* (44), 16206–16214.

(63) Yang, L.; Saavedra, S. S.; Armstrong, N. R. Sol-Gel-Based, Planar Waveguide Sensor for Gaseous Iodine. *Anal. Chem.* **1996**, *68* (11), 1834–1841. https://doi.org/10.1021/ac960033q.

(64) Bhowmik, B.; Jendrasiak, G. L.; Rosenberg, B. Charge Transfer Complexes of Lipids with Iodine. *Nat. Publ. Gr.* **1967**, *216*, 615–616.

(65) Walker, L. A.; Pullen, S.; Donovan, B.; Sension, R. J. On the Structure of Iodine Charge-Transfer Complexes in Solution. *Chem. Phys. Lett.* **1995**, *242* (1–2), 177–183. https://doi.org/10.1016/0009-2614(95)00683-U.

(66) Benesi, H. A.; Hildebrand, J. H. A Spectrophotometric Investigation of the Interaction of Iodine with Aromatic Hydrocarbons. *J. Am. Chem. Soc.* **1949**, *71* (8), 2703–2707. https://doi.org/10.1021/ja01176a030.

(67) Juang, C. B.; Finzi, L.; Bustamante, C. J. Design and Application of a Computer-Controlled Confocal Scanning Differential Polarization Microscope. *Rev. Sci. Instrum.* **1988**, *59* (11), 2399–2408. https://doi.org/10.1063/1.1139918.

(68) Blake, A. J.; Devillanova, F. A.; Gould, R. O.; Li, W. S.; Lippolis, V.; Parsons, S.; Radek, C.; Schröder, M. Template Self-Assembly of Polyiodide Networks. *Chem. Soc. Rev.* **1998**, *27* (3), 195–205. https://doi.org/10.1039/a827195z.

(69) De Miguel, M.; Ragon, F.; Devic, T.; Serre, C.; Horcajada, P.; García, H. Evidence of Photoinduced Charge Separation in the Metal-Organic Framework MIL-125(Ti)-NH2. *ChemPhysChem* **2012**, *13* (16), 3651–3654. https://doi.org/10.1002/cphc.201200411.

(70) Santaclara, J. G.; Nasalevich, M. A.; Castellanos, S.; Evers, W. H.; Spoor, F. C. M.; Rock, K.; Siebbeles, L. D. A.; Kapteijn, F.; Grozema, F.; Houtepen, A.; Gascon, J.; Hunger, J.; Van Der Veen, M. A. Organic Linker Defines the Excited-State Decay of Photocatalytic MIL-125(Ti)-Type Materials. *ChemSusChem* **2016**, *9* (4), 388–395. https://doi.org/10.1002/cssc.201501353.

(71) Li, Y.; Fu, Y.; Ni, B.; Ding, K.; Chen, W.; Wu, K.; Huang, X.; Zhang, Y. Effects of Ligand Functionalization on the Photocatalytic Properties of Titanium-Based MOF: A Density Functional

Theory Study. *AIP Adv.* **2018**, *8* (3). https://doi.org/10.1063/1.5021098.

(72) Matousek, P.; Everall, N.; Littlejohn, D.; Nordon, A.; Bloomfield, M. Dependence of Signal on Depth in Transmission Raman Spectroscopy. *Appl. Spectrosc.* **2011**, *65* (7), 724–733.

(73) Piryatinski, A.; Ivanov, S. A.; Tretiak, S.; Klimov, V. I. Effect of Quantum and Dielectric Confinement on the Exciton−Exciton Interaction Energy in Type II Core/Shell Semiconductor Nanocrystals. *Nano Lett.* **2007**, *7* (1), 108–115. https://doi.org/10.1021/nl0622404.

(74) Portnoi, M. E.; Galbraith, I. Ionization Degree of the Electron-Hole Plasma in Semiconductor Quantum Wells. *Phys. Rev. B* **1999**, *60* (8), 5570–5581. https://doi.org/10.1103/PhysRevB.60.5570.

(75) Takagahara, T. Biexciton States in Semiconductor Quantum Dots and Their Nonlinear Optical Properties. *Phys. Rev. B* **1989**, *39* (14), 10206–10231. https://doi.org/10.1103/PhysRevB.39.10206.

(76) Chen, C.; Li, X.; Zou, W.; Wan, H.; Dong, L.; Guan, G. Structural Modulation of UiO-66-NH2 Metal-Organic Framework via Interligands Cross-Linking: Cooperative Effects of Pore Diameter and Amide Group on Selective CO2 Separation. *Appl. Surf. Sci.* **2021**, *553* (November 2020), 149547. https://doi.org/10.1016/j.apsusc.2021.149547.

(77) Katz, M. J.; Brown, Z. J.; Colón, Y. J.; Siu, P. W.; Scheidt, K. A.; Snurr, R. Q.; Hupp, J. T.; Farha, O. K. A Facile Synthesis of UiO-66, UiO-67 and Their Derivatives. *Chem. Commun.* **2013**, *49* (82), 9449–9451. https://doi.org/10.1039/C3CC46105J.

Figure 1: Structural disorder (a) of the carbon atoms of the aromatic rings of the linker and (b) of the $-NH_2$ function. Structural representation (c) of an hexameric $M_6O_4(OH)_4(NH_2-BPDC)_{12}$ node, and (d) of the UiO-67_NH_2 network (in this last case hydrogen and nitrogen atoms have been omitted for clarity).

Figure 2: N_2 sorption isotherms at 77K, for UiO-67_NH_2(Zr) (black), UiO-67_NH_2(Zr/Hf) (red) and UiO-67_NH_2(Hf) (blue) degassed at 60 ºC. The SSA values obtained using the BET method are also displayed.

Figure 3: On the left: SEM images of UiO-67_NH_2(Zr) (on top), UiO-67_NH_2(Zr/Hf) (in the middle), and UiO-67_NH_2(Hf) (on bottom). On the right: SEM-EDS layered images, elemental mapping, and EDS spectra. In green: $Zr_{L\alpha1}$. In red: $Hf_{M\alpha1}$.

Figure 4: Raman spectra collected with a wavelength excitation of 785 nm (top) and FTIR spectra (bottom) for UiO-67_NH_2(Zr) (black), UiO-67_NH_2(Zr/Hf) (red), and UiO-67_NH_2(Hf) (blue) compounds.

Figure 5: UV-vis spectra of UiO-67_NH_2(Zr) (black), UiO-67_NH_2(Zr/Hf) (red), and UiO-67_NH_2(Hf) (blue) materials. Inset: Tauc plot considering that a given UiO-67_NH_2(Zr,Hf) sample is defined either by direct (straight lines) or an indirect (dotted lines) transition.

Figure 6: Adsorption kinetics of iodine after 48 h of contact for the UiO-67_NH_2(Zr) (black), UiO-67_NH_2(Zr/Hf) (red), and UiO-67_NH_2(Hf) (blue) samples.

Figure 7: UV-vis spectra obtained for UiO-67_NH_2(Zr,Hf) materials after 48 h of iodine exposure. In black: I_2@UiO-67_NH_2(Zr), in red: I_2@UiO-67_NH_2(Zr/Hf), and in blue: I_2@UiO-67_NH_2(Hf). The samples were mixed with $BaSO_4$ in a concentration of 3% before the analysis. The position of the lasers' wavelength used for the Raman mapping are also highlighted in the figure.

Figure 8: Non-resonance Raman mappings (λ_{ex} = 785 nm) over UiO-67_NH_2(Zr), UiO-67_NH_2(Zr/Hf), and UiO-67_NH_2(Hf) crystals obtained after 16 h of iodine loading. The average spectra obtained by all the collected single spectrum at different XY points for the same crystal are displayed in the top of the figure. (a)

spatial distribution of the "perturbed" I_2 – green region in the average spectra (centered at 170 cm^{-1}) –; (b) spatial distribution of the I_3^- – blue region in the average spectra (centered at 107 cm^{-1}). The colors in the maps are representative of the intensity of the signal, going from blue (less intense) up to red-brown (most intense).

Figure 9: Non-resonance Raman mappings (λ_{ex} = 785 nm) over UiO-67_NH$_2$(Zr), UiO-67_NH$_2$(Zr/Hf), and UiO-67_NH$_2$(Hf) crystals obtained after 48 h of iodine loading. The average spectra obtained by all the collected single spectrum at different XY points for the same crystal are displayed in the top of the figure. (a) spatial distribution of the "perturbed" I_2 – green region in the average spectra (centered at 170 cm^{-1}) –; (b) spatial distribution of the I_3^- – blue region in the average spectra (centered at 107 cm^{-1}). The colors in the maps are representative of the intensity of the signal, going from blue (less intense) up to red-brown (most intense).

Figure 10: Resonance Raman mappings (λ_{ex} = 515 nm) over UiO-67_NH$_2$(Zr), UiO-67_NH$_2$(Zr/Hf), and UiO-67_NH$_2$(Hf) crystals obtained after 16 h of iodine loading. The average spectra obtained by all the collected single spectrum at different XY points for the same crystal are displayed in the top of the figure. (a) spatial distribution of the "perturbed" I_2 – green region in the average spectra (centered at 170 cm^{-1}) –; (b) spatial distribution of the I_3^- – blue region in the average spectra (centered at 107 cm^{-1}). The colors in the maps are representative of the intensity of the signal, going from blue (less intense) up to red-brown (most intense).

Figure 11: Resonance Raman mappings (λ_{ex} = 515 nm) over UiO-67_NH$_2$(Zr), UiO-67_NH$_2$(Zr/Hf), and UiO-67_NH$_2$(Hf) crystals obtained after 48 h of iodine loading. The average spectra obtained by all the collected single spectrum at different XY points for the same crystal are displayed in the top of the figure. (a) spatial distribution of the "perturbed" I_2 – green region in the average spectra (centered at 170 cm^{-1}) –; (b) spatial distribution of the I_3^- – blue region in the average spectra (centered at 107 cm^{-1}). The colors in the maps are representative of the intensity of the signal, going from blue (less intense) up to red-brown (most intense)

Figure 12: Non resonance Raman cartography over a UiO-67_NH$_2$(Zr/Hf) crystal performed in three dimensions ($0 \leq x \leq 205.5$ μm; $0 \leq y \leq 202.3$ μm; $0 \leq z \leq 105$ μm) at λ_{ex} = 785 nm. On top: The average spectra obtained by all the collected single spectrum at different XYZ points. In the middle: spatial distribution of the "perturbed" I_2 (green region in the average spectra). On bottom: spatial distribution of the I_3^- (blue

region in the average spectra). The 2D cartographies display the XY plan in different depths. The 3D intensity map is highlighted in the left side alongside one slice of the XZ (middle) and YZ (right) plans.

TABLE CAPTIONS

Table 1: Resume of the physical chemical properties for the UiO-67_NH$_2$(Zr,Hf) compounds.

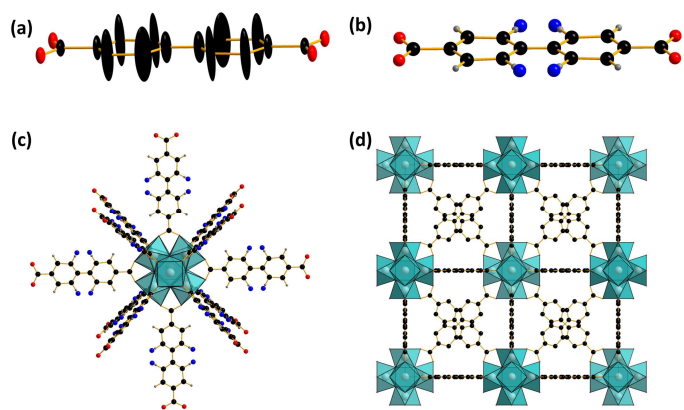**Table 2:** Summary of the physical chemical properties for the iodine loaded UiO-67_NH$_2$(Zr,Hf) compounds.
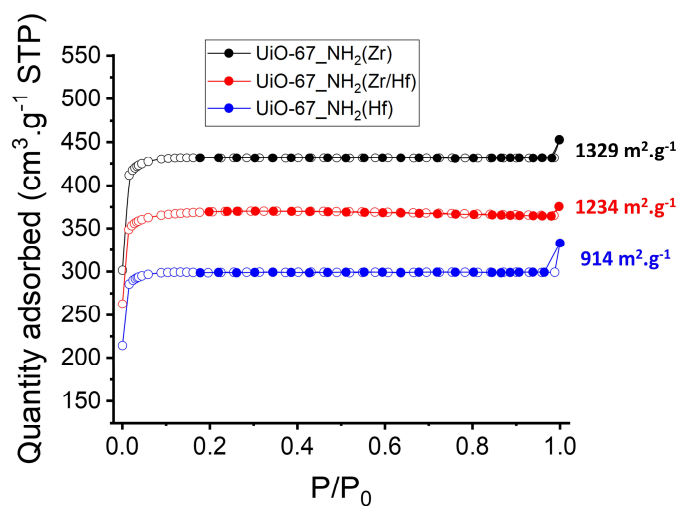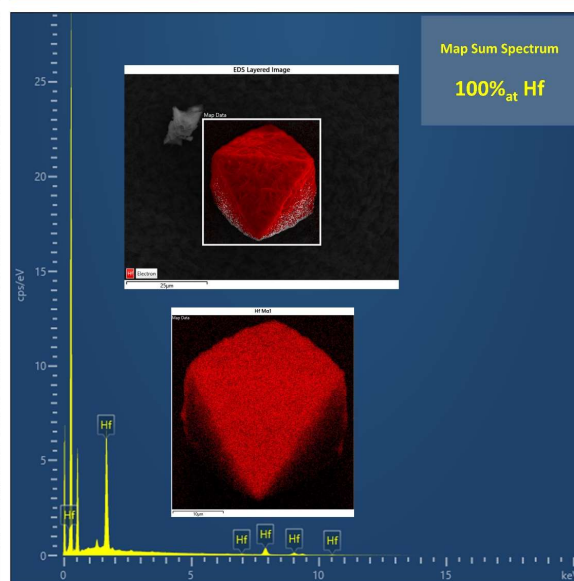
FIGURE 1

FIGURE 2

FIGURE 3
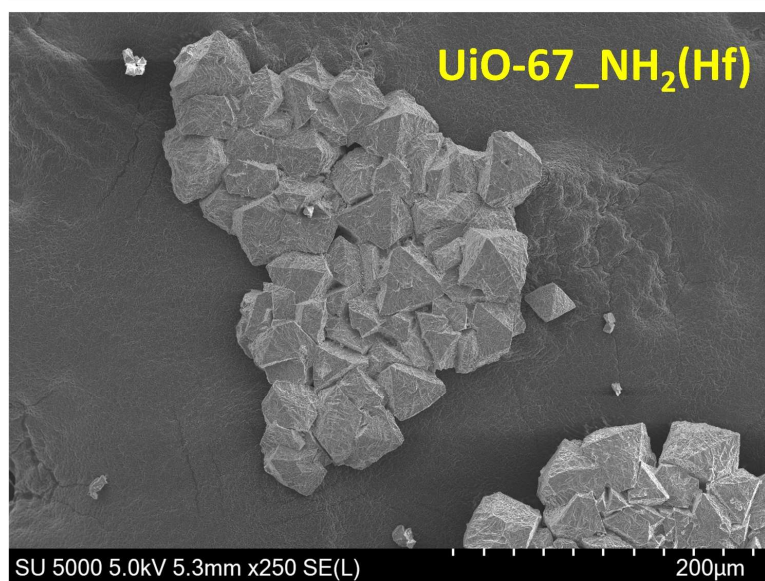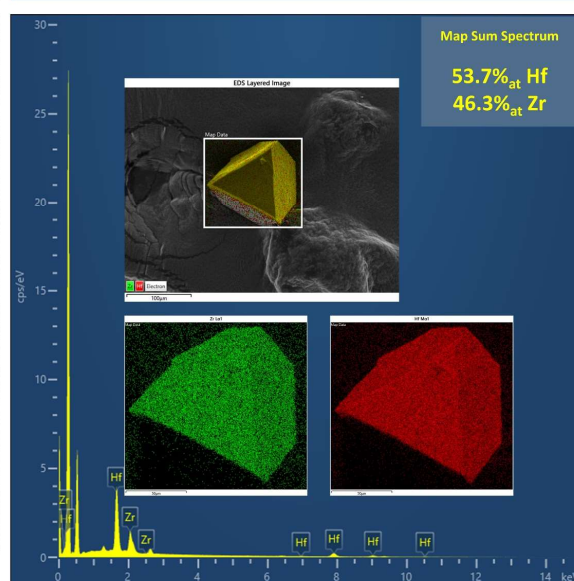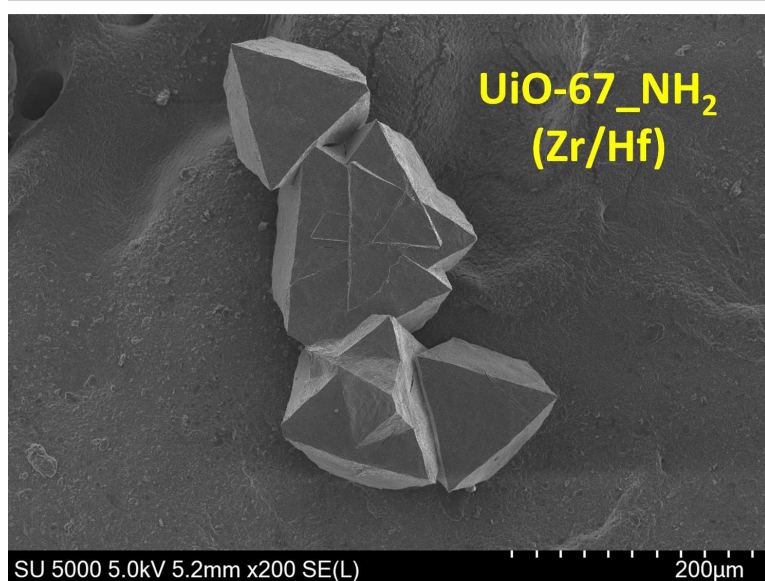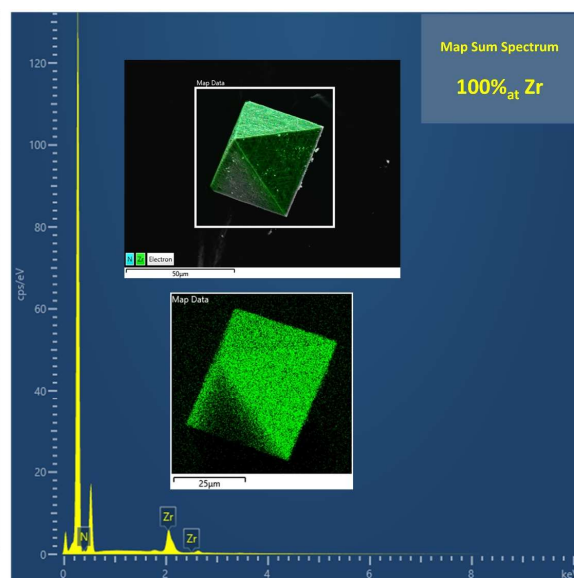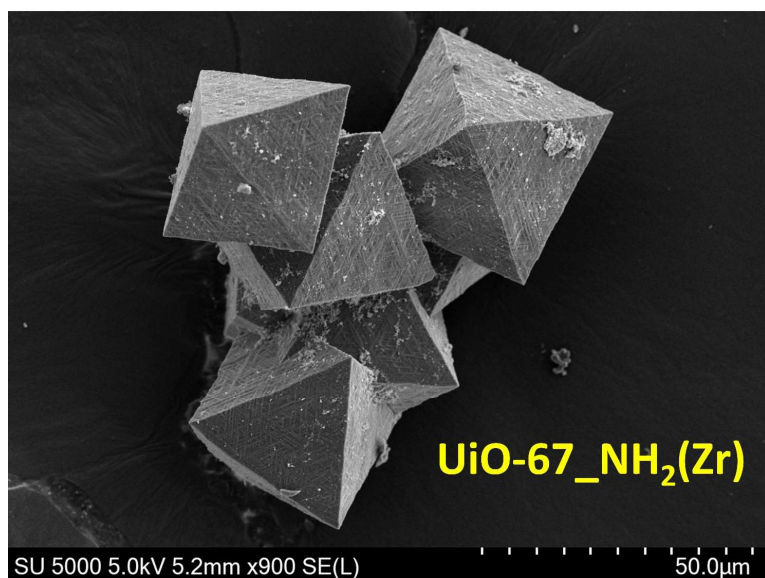
FIGURE 4
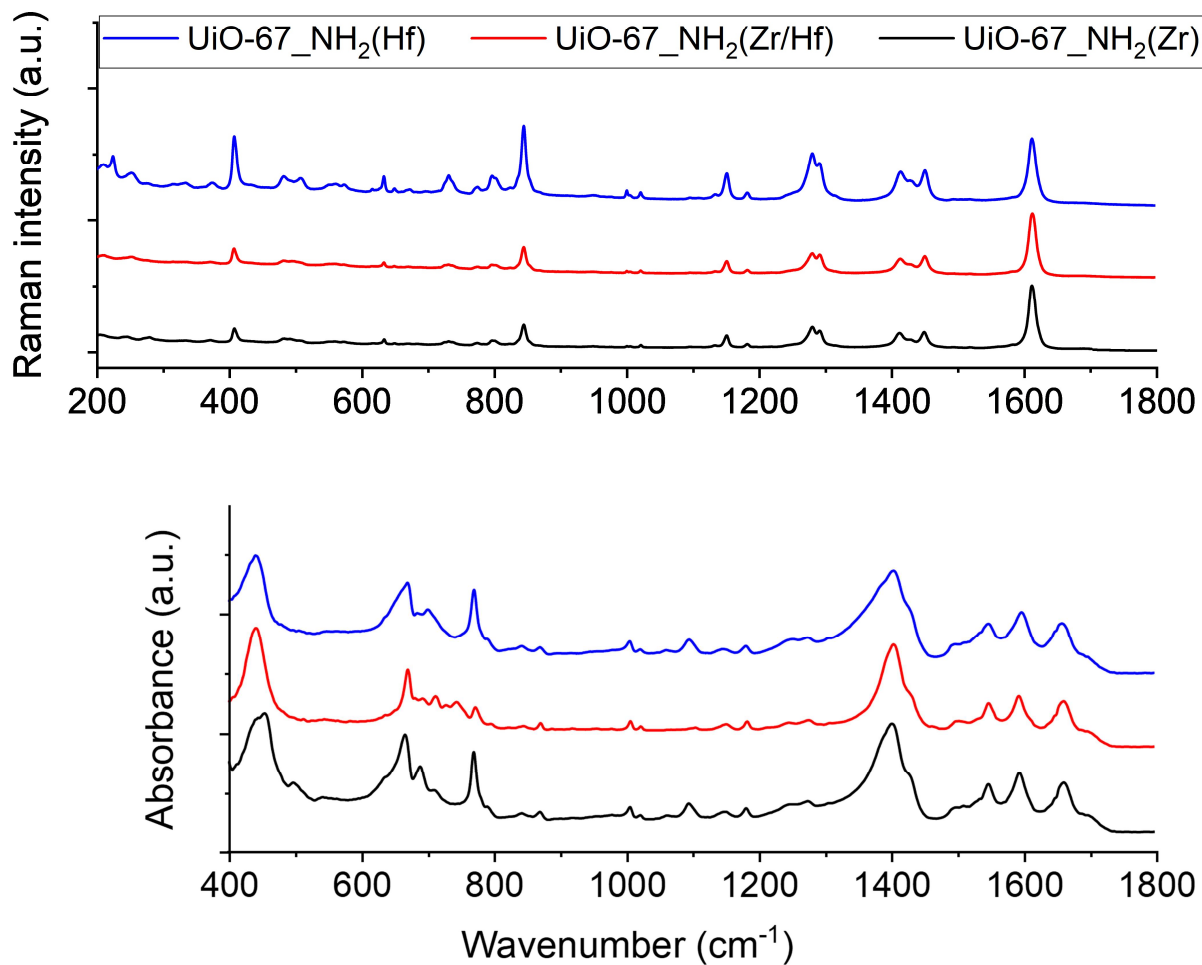
FIGURE 5
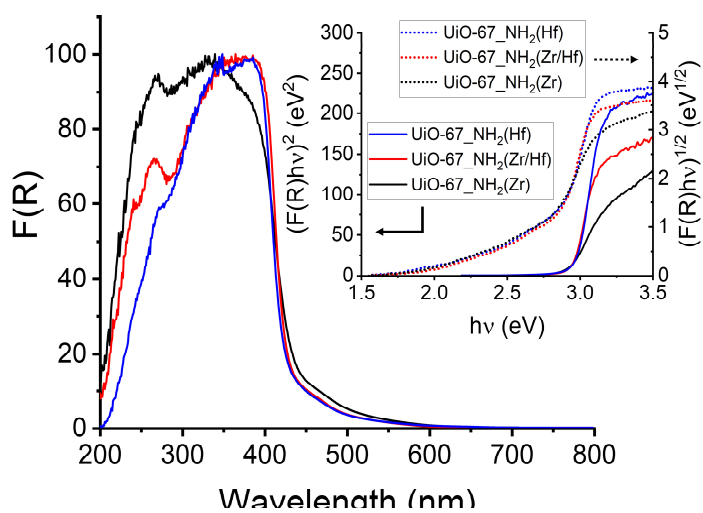
FIGURE 6
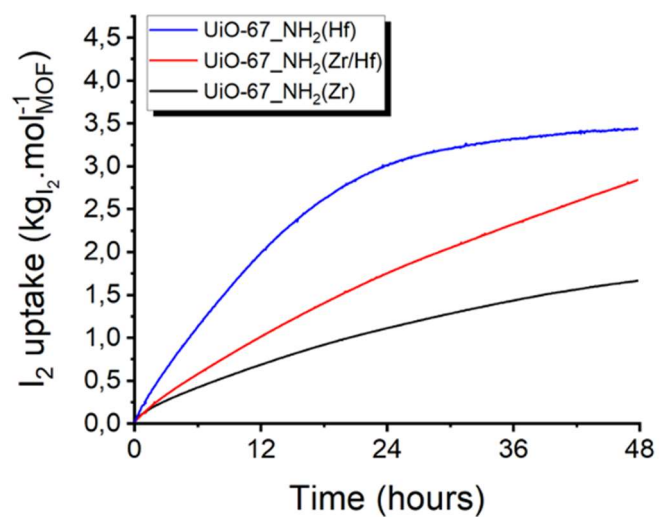
FIGURE 7

FIGURE 8

FIGURE 9

UiO-67_NH$_2$(Zr) UiO-67_NH$_2$(Zr/Hf) UiO-67_NH$_2$(Hf)

(a)

(b)

46
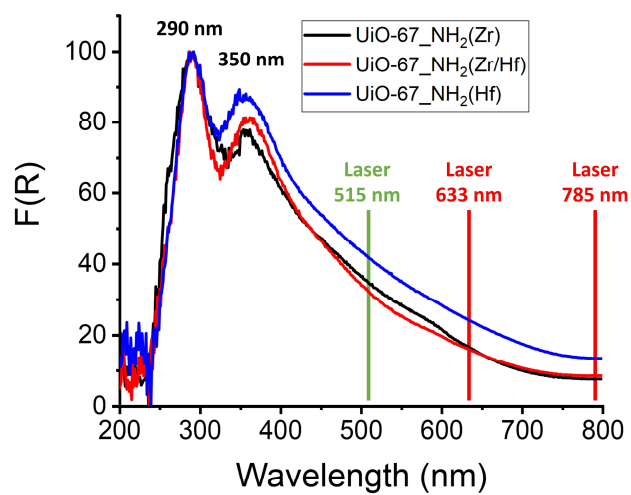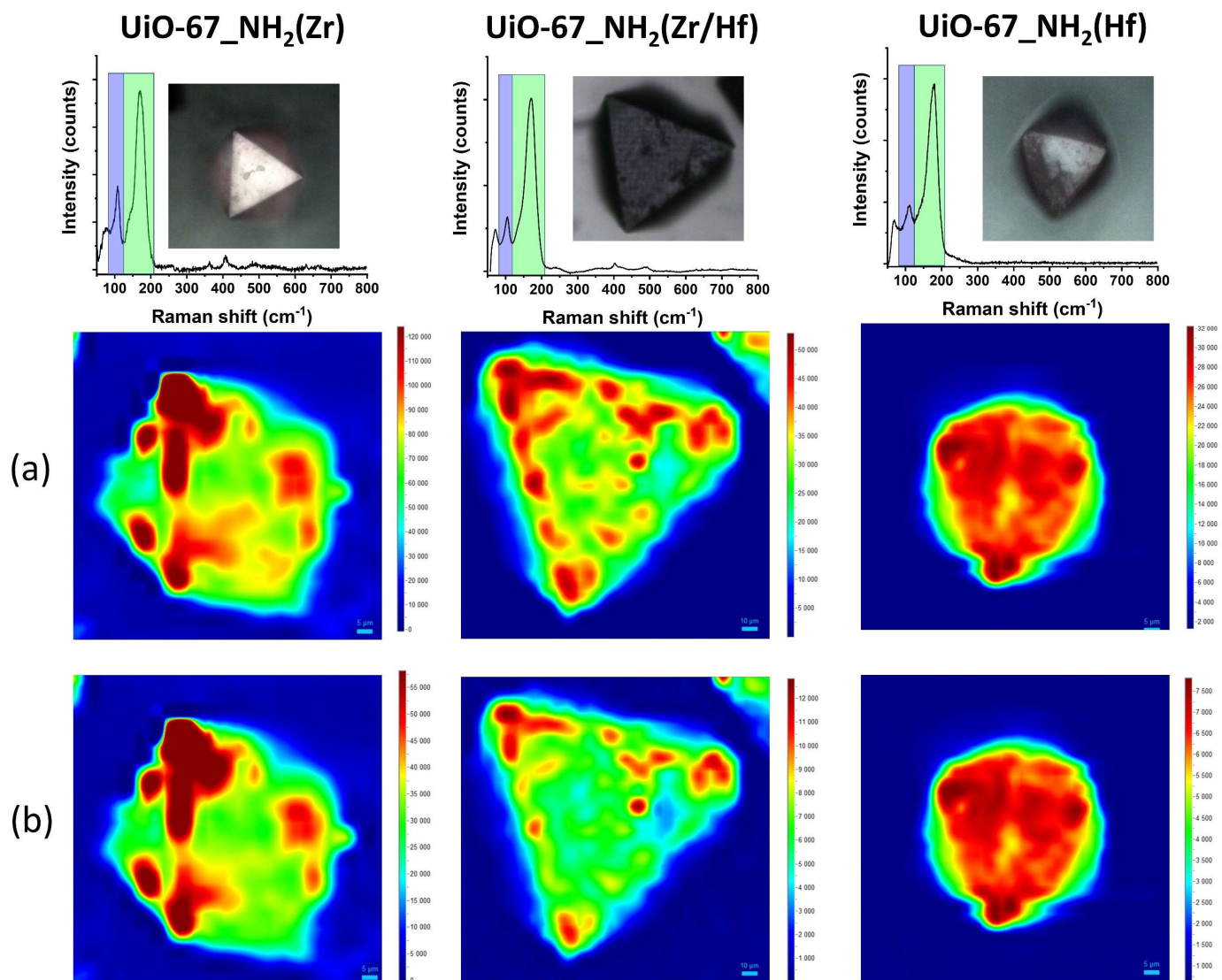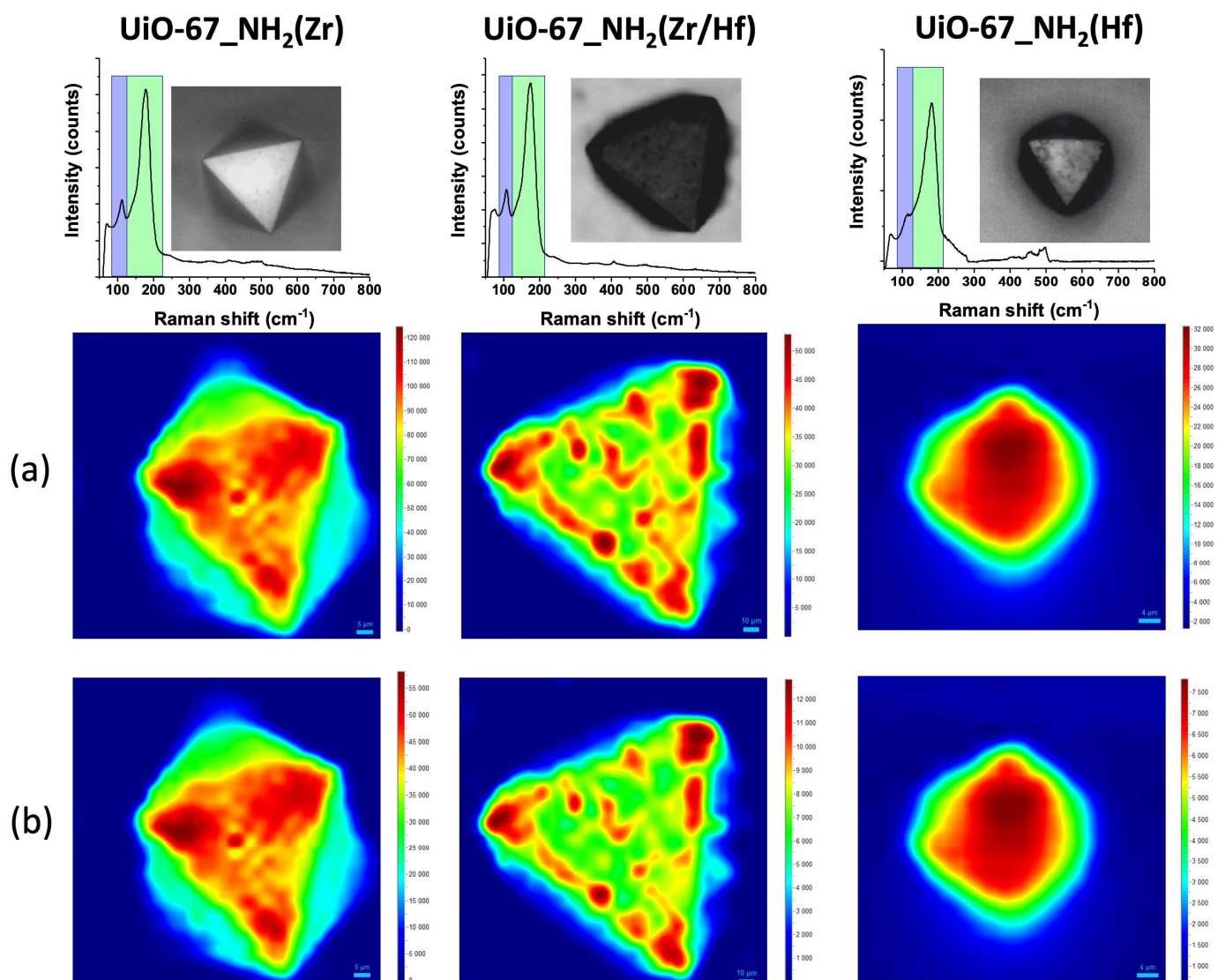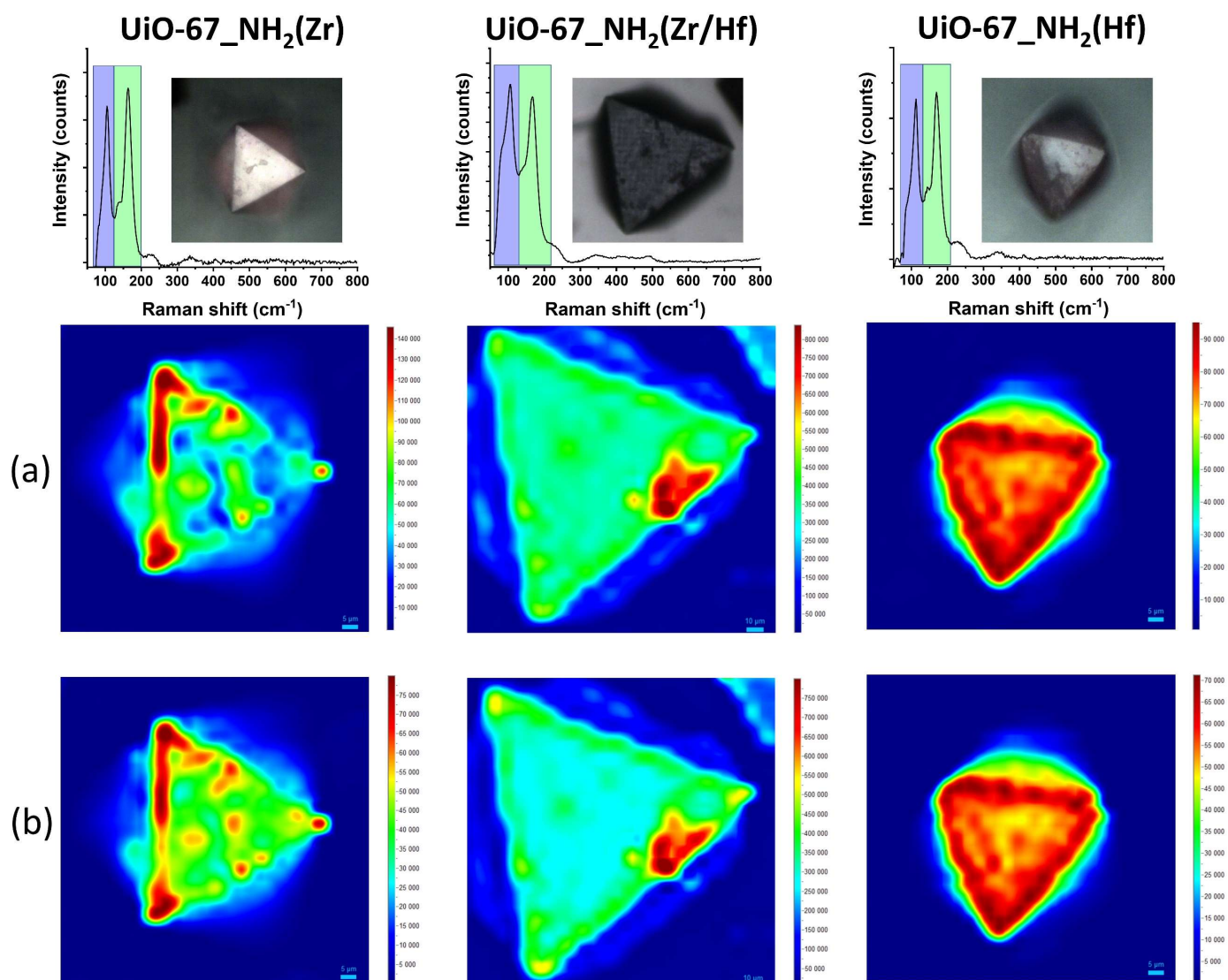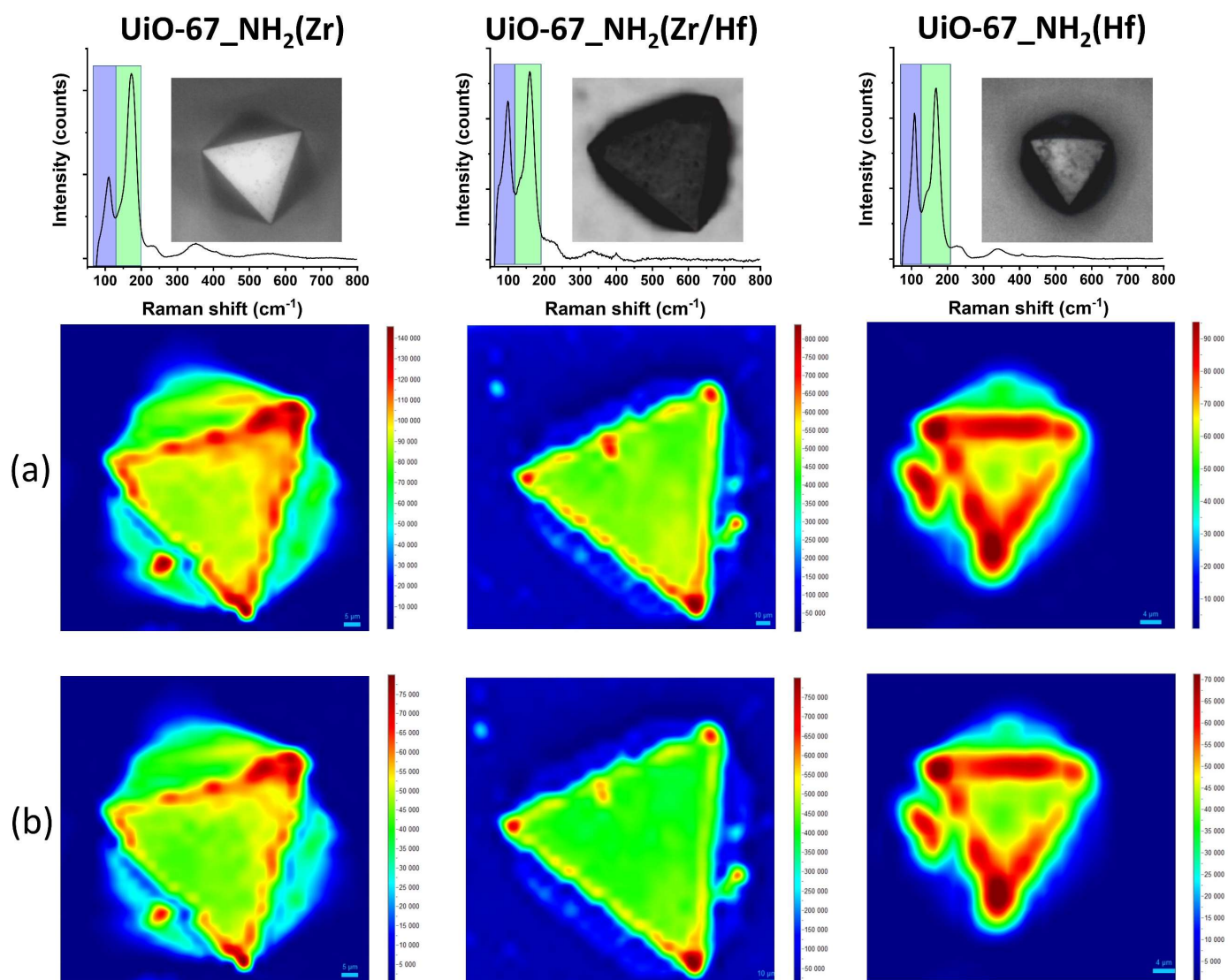
FIGURE 10

FIGURE 11

FIGURE 12
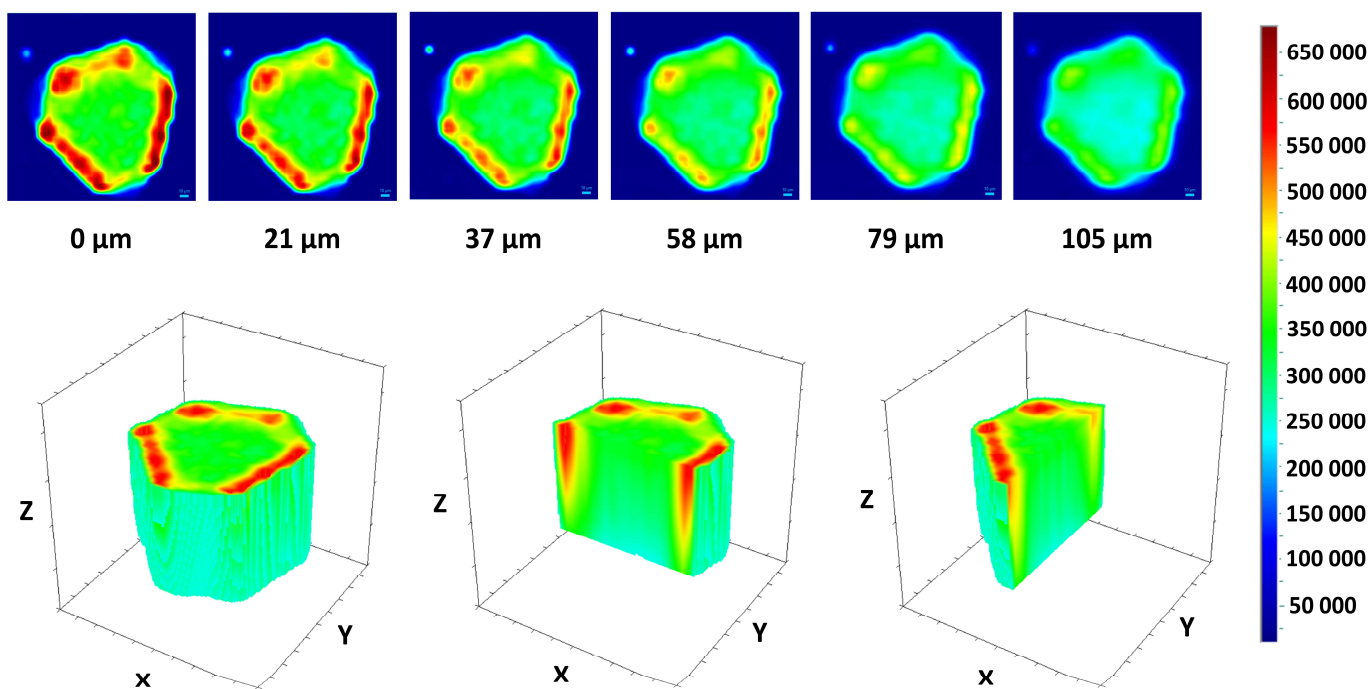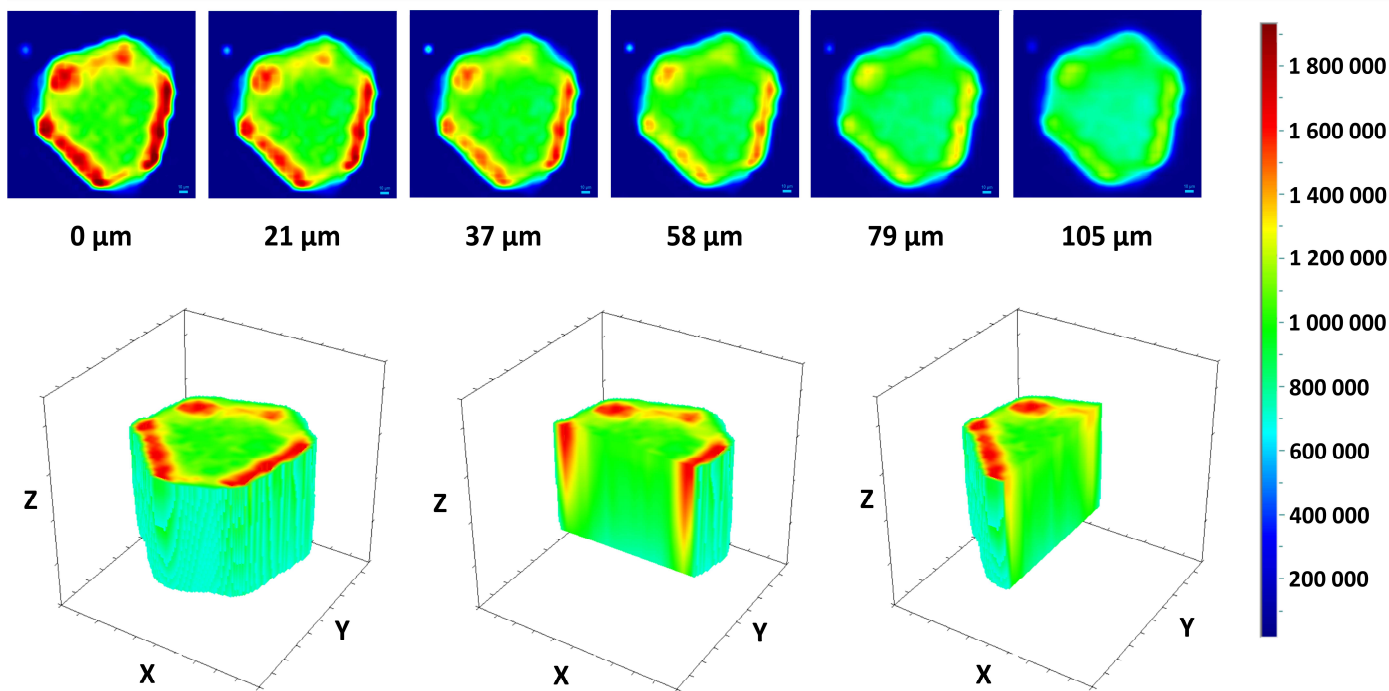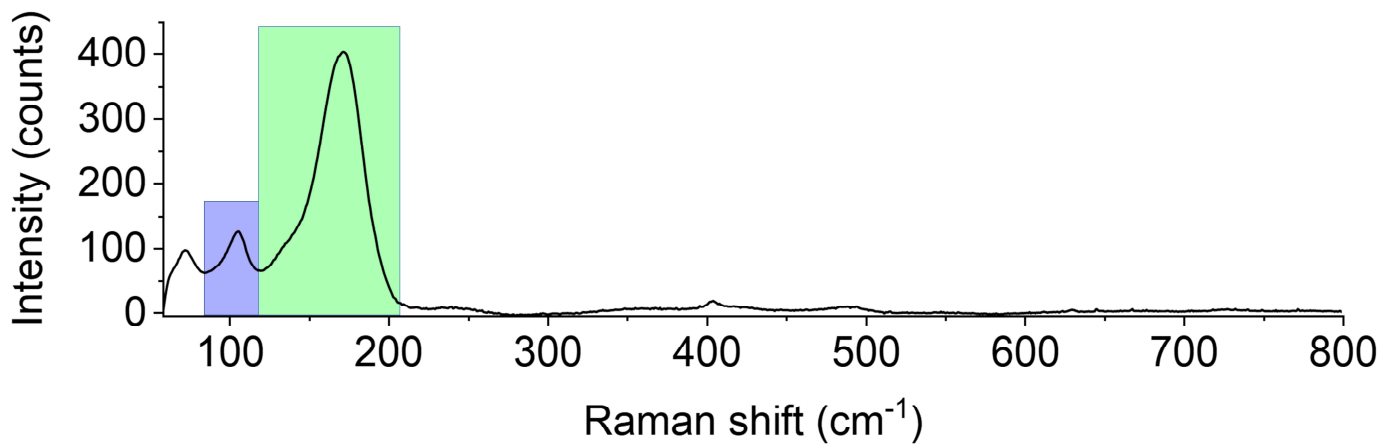
TABLE 1

MOF	Metal content			Crystal size	SSA$_{(BET)}$	Microporous volume	Missing NH$_2$–BPDC linker defects
Metal	ICP-OES	SC-XRD	EDS	(μm)	(m^2.g^{-1})	(cm^3.g^{-1})	(%)
Zr	100%$_{at}$ Zr	100%$_{at}$ Zr	100%$_{at}$ Zr	32 – 51	1329 ± 36	0.68(4)	10.3
Zr/Hf	40.0%$_{at}$ Zr 60.0%$_{at}$ Hf	46.3%$_{at}$ Zr 53.7%$_{at}$ Hf	46.0%$_{at}$ Zr 54.0%$_{at}$ Hf	105 – 140	1234 ± 34	0.65(7)	5.5
Hf	100%$_{at}$ Hf	100%$_{at}$ Hf	100%$_{at}$ Hf	24 – 44	914 ± 25	0.48(4)	8.0

TABLE 2

UiO-67_NH$_2$(M)	I$_2$ uptake capacity after 16 h		I$_2$ uptake capacity after 48 h		k_{LDF}	R^2
(M)	(mg.g^{-1})	(g.mol^{-1})	(mg.g^{-1})	(g.mol^{-1})	(h^{-1})	
Zr	376[a]	832[a]	749[a]	1658[a]	0.0487(2)	0.977
Zr/Hf	533	1263	1196	2835	0.0427(2)	0.968
Hf	885[a]	2419[a]	1254[a]	3428[a]	0.0778(3)	0.988

[a] not saturated kinetic curve at t = 48h; k_{LDF} = mass transfer coefficient from the linear drive force (LDF) model [$F(t)$ = 1 − exp[−$k_{LDF}t$]); R^2 = correlation coefficient.